NREL
NATIONAL RENEWABLE ENERGY LABORATORY

LIDAR Wind Speed Measurements of Evolving Wind Fields

E. Simley and L.Y. Pao
University of Colorado
Boulder, Colorado

NREL Technical Monitor: Alan Wright

NREL is a national laboratory of the U.S. Department of Energy, Office of Energy Efficiency & Renewable Energy, operated by the Alliance for Sustainable Energy, LLC.

Subcontract Report
NREL/SR-5000-55516
July 2012

Contract No. DE-AC36-08GO28308

NREL
NATIONAL RENEWABLE ENERGY LABORATORY

LIDAR Wind Speed Measurements of Evolving Wind Fields

E. Simley and L.Y. Pao
University of Colorado
Boulder, Colorado

NREL Technical Monitor: Alan Wright
Prepared under Subcontract No. XEE-1-11300-01

National Renewable Energy Laboratory
15013 Denver West Parkway
Golden, Colorado 80401
303-275-3000 • www.nrel.gov

Subcontract Report
NREL/SR-5000-55516
July 2012

Contract No. DE-AC36-08GO28308

This publication received minimal editorial review at NREL.

NOTICE

Available electronically at http://www.osti.gov/bridge

Available for a processing fee to U.S. Department of Energy
and its contractors, in paper, from:

U.S. Department of Energy
Office of Scientific and Technical Information
P.O. Box 62
Oak Ridge, TN 37831-0062
phone: 865.576.8401
fax: 865.576.5728
email: mailto:reports@adonis.osti.gov

Available for sale to the public, in paper, from:

U.S. Department of Commerce
National Technical Information Service
5285 Port Royal Road
Springfield, VA 22161
phone: 800.553.6847
fax: 703.605.6900
email: orders@ntis.fedworld.gov
online ordering: http://www.ntis.gov/help/ordermethods.aspx

Cover Photos: (left to right) PIX 16416, PIX 17423, PIX 16560, PIX 17613, PIX 17436, PIX 17721

Printed on paper containing at least 50% wastepaper, including 10% post consumer waste.

LIDAR Wind Speed Measurements of Evolving Wind Fields

E. Simley and L. Y. Pao

Abstract

Light Detection and Ranging (LIDAR) systems are able to measure the speed of incoming wind before it interacts with a wind turbine rotor. These preview wind measurements can be used in feedforward control systems that are designed to reduce turbine loads. However, the degree to which such preview-based control techniques can reduce loads by reacting to turbulence depends on how accurately the incoming wind field can be measured. Past studies have assumed the validity of physicist G.I. Taylor's 1938 frozen turbulence hypothesis, which implies that turbulence remains unchanged as it advects downwind at the mean wind speed. With Taylor's hypothesis applied, the only source of wind speed measurement error is distortion caused by the LIDAR. This study introduces wind evolution, characterized by the longitudinal coherence of the wind, to LIDAR measurement simulations using the National Renewable Energy Laboratory's (NREL's) 5-megawatt turbine model to create a more realistic measurement model. A simple model of wind evolution was applied to a frozen wind field that was used in previous studies to investigate the effects of varying the intensity of wind evolution. LIDAR measurements were also evaluated using a large eddy simulation (LES) of a stable boundary layer that was provided by the National Center for Atmospheric Research.

The LIDAR measurement scenario investigated consists of a hub-mounted LIDAR that scans a circle of points upwind of the turbine in order to estimate the wind speed component in the mean wind direction. Different combinations of the preview distance that is located upwind of the rotor and the radius of the scan circle were analyzed. It was found that the dominant source of measurement error for short preview distances is the detection of transverse and vertical wind speeds from the line-of-sight LIDAR measurement. It was discovered in previous studies that, in the absence of wind evolution, the dominant source of error for large preview distances is the spatial averaging caused by the LIDAR's sampling volume. However, by introducing wind evolution, the dominant source of error for large preview distances was found to be the coherence loss caused by evolving turbulence. Different measurement geometries were compared using the bandwidth for which the measurement coherence remained above 0.5 and also the area under the measurement coherence curve. Results showed that, by increasing the intensity of wind evolution, the measurement coherence decreases. Using the coherence bandwidth metric, the optimal preview distance for a fixed-scan radius remained almost constant for low and moderate amounts of wind evolution. For the wind field with the simple wind evolution model introduced, the optimal preview distance for a scan radius of 75% blade span (47.25 meters) was found to be 80 meters. Using the LES wind field, the optimal preview distance was 65 meters. When comparing scan geometries using the area under the coherence curve, results showed that, as the intensity of wind evolution increases, the optimal preview distance decreases.

List of Acronyms, Abbreviations, and Nomenclature

a	Decay parameter for exponential coherence
a_l	Decrement parameter for transverse coherence ($l \in \{u, v, w\}$)
b_l	Offset parameter for transverse coherence ($l \in \{u, v, w\}$)
D	Longitudinal distance between two points or measurement preview distance
F	Focal distance
f	Frequency (Hertz)
θ	LIDAR measurement angle away from longitudinal direction
k	Wind velocity wavenumber (m^{-1})
λ	Eddy wavelength (meters)
R	Range along LIDAR beam
r	Scan radius for spinning LIDAR scenario
$r_{i,j}$	Distance between two points in the *yz* plane
U	Mean wind speed (meters/second)
$\bar{u}_{i,j}$	Average mean wind speed between two points in the *yz* plane
ψ	Azimuth angle in rotor plane
$\gamma_{xy}^2(f)$	Coherence between signals *x* and *y*
$S_{xx}(f)$	Power spectral density (PSD) of signal *x*
$S_{xy}(f)$	Cross-power spectral density (CPSD) between signals *x* and *y*
CPSD	Cross-power spectral density
CW	Continuous wave (a class of Light Detection and Ranging devices)
LES	Large eddy simulation
LIDAR	Light Detection and Ranging
MW	Megawatt
NCAR	National Center for Atmospheric Research
NREL	National Renewable Energy Laboratory
PSD	Power spectral density
RMS	Root mean square (the square root of the mean of the square of a signal)

Contents

List of Figures

List of Tables

1 Introduction

Wind speed measurements in front of a wind turbine can be used as part of feedforward or preview-based controllers to help mitigate structural loads that are caused by turbulent wind conditions. Prior analyses have shown that reductions in turbine loads can be achieved with knowledge of the incoming wind field [1, 2, 3]. A block diagram of such a control strategy is shown in Figure 1. Upstream wind is measured, indicated by the Light Detection and Ranging (LIDAR) system block, which provides an estimate of the wind speeds that will eventually reach the turbine after a delay time of D/U, where D is the preview distance between the rotor and the measurement location and U is the mean wind speed. In reality, the turbulent structures in the wind will evolve between the time they are measured and when they reach the turbine, causing errors in the preview wind measurements [4]. Since wind evolution is caused by physical properties of the atmosphere that can only be estimated, it is represented as part of the "plant" of the control system architecture. Wind evolution and LIDAR blocks are shown as part of the control system because their known and estimated effects will have an impact on how the controller is designed.

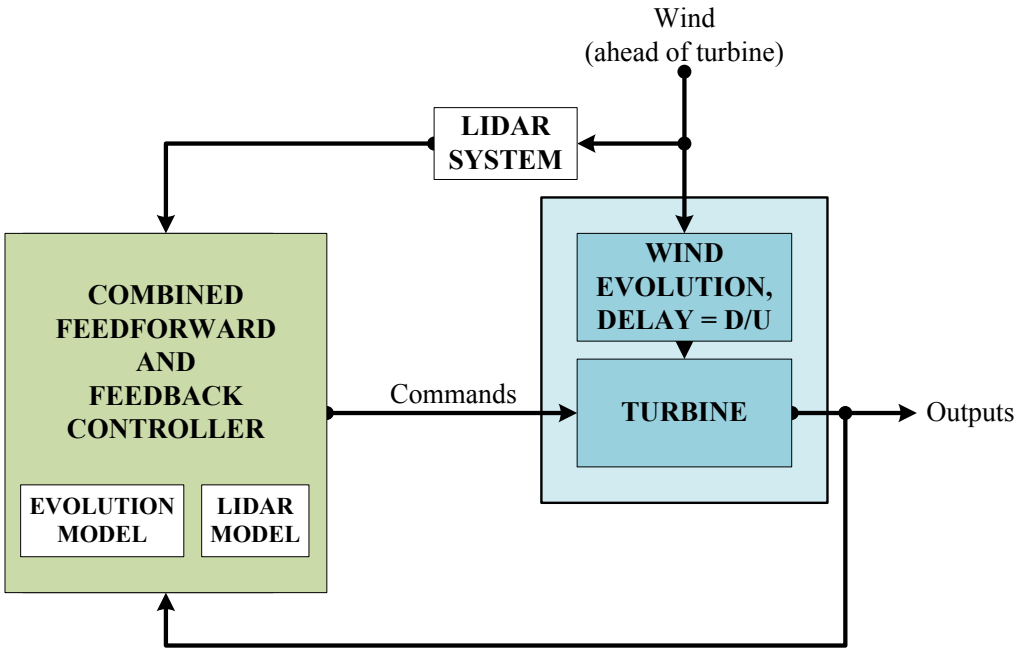

Figure 1. A block diagram illustrating how LIDAR is used in a preview-based combined feedforward/feedback control scenario. The wind evolution block represents the coherence loss between wind at the measurement location and the wind encountered by the rotor after a delay time of *D*/*U*. The distance *D* is the distance upwind of the rotor where the measurement is taken and *U* is the mean wind speed.

Previous work combining preview measurement-based control systems and LIDAR models [5, 6] assumed the validity of physicist G.I. Taylor's 1938 frozen turbulence hypothesis [7], which claims that turbulent eddies remain unchanged while advecting with the average wind velocity. In this report, we combine our existing model [8] of LIDAR measurements with models of wind evolution. The goal was to study the degree in which wind inflow can be accurately measured and to determine which scenarios provide the best measurements.

In addition to wind evolution, another source of wind distortion exists—the induction zone of the turbine. The induction zone has the effect of slowing down the mean velocity of the wind near the rotor and altering the turbulence characteristics [9]. The important topic of wind inflow distortion is an area of future research and is not addressed in this report, where only the effects of freestream wind evolution were considered.

Wind evolution is described here as the coherence between wind speeds at two points that are separated longitudinally (in the mean wind direction) in the flow. Taylor's hypothesis regarding frozen wind fields suggests a coherence function of one at all frequencies for all purely longitudinal separations. Wind speeds at two locations separated longitudinally would simply be delayed versions of each other, with a delay time of D/U. Introducing wind evolution to a frozen wind field involves applying a coherence function to the wind at locations that are separated longitudinally, in addition to the transverse coherence already provided by most wind models. Throughout this report, "transverse" is used to identify the *yz* plane that is perpendicular to the mean wind direction, not just the *y*, or horizontal, direction that is perpendicular to the wind flow.

In this report, researchers investigate LIDAR measurement quality for realistic LIDAR scanning scenarios in evolving wind fields. Two types of evolving wind fields are used for measurement analysis. First, a frozen, or non-evolving, wind field was generated using the National Renewable Energy Laboratory's (NREL's) TurbSim [10] code. The code is coupled with a simple longitudinal coherence model to create an evolving wind field. The longitudinal coherence model can be adjusted to simulate varying degrees of wind evolution. Second, a wind field based on large eddy simulation (LES) of the stable boundary layer generated by the National Center for Atmospheric Research (NCAR) [11] was studied. Since the LES wind field includes physics-based wind evolution, a separate model of longitudinal coherence does not need to be applied. Using these two types of wind fields, researchers analyzed LIDAR measurement quality for different measurement geometries by calculating the coherence between the measured wind and the evolved wind that reaches the turbine rotor plane. Instead of directly simulating LIDAR measurements in four-dimensional wind fields, the spectra of the wind and the transverse and longitudinal coherence functions were used to calculate the overall measurement coherence.

A previous study by the authors [8] examined the effects of LIDAR on measurement error for realistic scenarios involving NREL's 5-megawatt (MW) wind turbine model [12] with frozen wind fields that were generated by TurbSim, including the wind field that is coupled with a model of wind evolution in this report. Emphasis was placed on a hub-mounted LIDAR scenario, where the LIDAR scanned a circle of wind in front of the rotor. Researchers found that, for a continuous-wave (CW) LIDAR model, there is an optimal preview distance for each scan radius where the minimum measurement error is achieved (see Figure 2 for a depiction of the preview distance, D, and scan radius, r). For a scan radius of 75% blade span [47.25 meters (m) for the 5-MW model], which is a radius of particular interest because of maximum power capture [1, 2, 3], optimal preview distances are near 150 m. In this report, more realistic achievable measurement errors and optimal preview distances are provided for the same measurement scenarios, with wind evolution incorporated.

This report is organized as follows. In Section 2, the principal equation used in the CW LIDAR model, called the "range weighting function," is presented, as well as the process through which

the longitudinal component of wind speed is estimated from a line-of-sight measurement. The ways in which range weighting and measurement geometry cause measurement errors are discussed here. Results from a realistic hub-mounted LIDAR measurement simulation are provided in Section 2.3, revealing the performance that can be expected in the absence of wind evolution. An introduction to coherence and an explanation of how a wind field can be described using coherence functions is provided in Section 3. In Section 4, the wind fields and wind evolution models examined are discussed, starting with a summary of the frozen wind field that was generated using the Great Plains-Low Level Jet model in TurbSim. The simple longitudinal coherence model used to introduce wind evolution to the frozen TurbSim wind field is described next. Section 4.3 includes a description of the stable LES wind field. In Section 5, the calculations used to determine the coherence between a LIDAR wind speed measurement and the wind that actually reaches the turbine rotor are derived. Section 6 includes results for measurement coherence using the calculations that were derived in Section 5 for the two wind field scenarios as functions of scan radius and preview distance. Finally, Section 7 concludes the report with a discussion of the coherence models and simulation results, and includes areas of future research.

2 LIDAR Measurements

The analysis of Light Detection and Ranging (LIDAR) system performance examined here uses the coordinate system shown in Figure 2. The ground referenced *x*, *y*, and *z* axes are defined such that -*z* is pointing in the direction of gravity and *x* is nominally pointing in the downwind direction. The wind speed vector is defined by *u*, *v*, and *w* components, where *u* is the streamwise component. Nominally, the *u*, *v*, and *w* axes are aligned with the *x*, *y*, and *z* axes, respectively, since the mean wind direction of the wind fields is in the *x* direction. The 5-megawatt (MW) wind turbine model, which our measurement geometry is based on, has a hub height of 90 meters (m) and a rotor diameter of 126 m.

The LIDAR measurement model that was created introduces two imperfections to wind speed measurements. Range weighting is the effect inherent to continuous-wave (CW) and pulsed LIDAR that acts as a spatial filter along the laser beam, thereby causing wind speeds at locations other than the focal distance to contribute to the measured value. The other primary source of error in wind speed measurements is due to estimating the *u* component of the wind velocity vector given a single line-of-sight measurement. This estimation problem is sometimes called the "cyclops dilemma." Control systems utilizing preview wind speed measurements primarily focus on the component of the wind that is perpendicular to the rotor plane, nominally the *u* component. The assumption is that the rotor plane is always perpendicular to the *x* axis. Therefore, the LIDAR measurements estimate the component of wind aligned with the *x* axis, which will be treated as equivalent to the *u* component for the rest of the report. When the LIDAR is staring in the *x* direction, there will be no geometrical measurement errors because the *v* and *w* components do not contribute to the detected radial velocity. If the laser is instead pointing in a direction other than parallel to the *x* axis, unknown *v* and *w* components will contribute to the measurement and an estimate of the *u* component must be formed. This latter source of error is referred to as "directional bias" in this report.

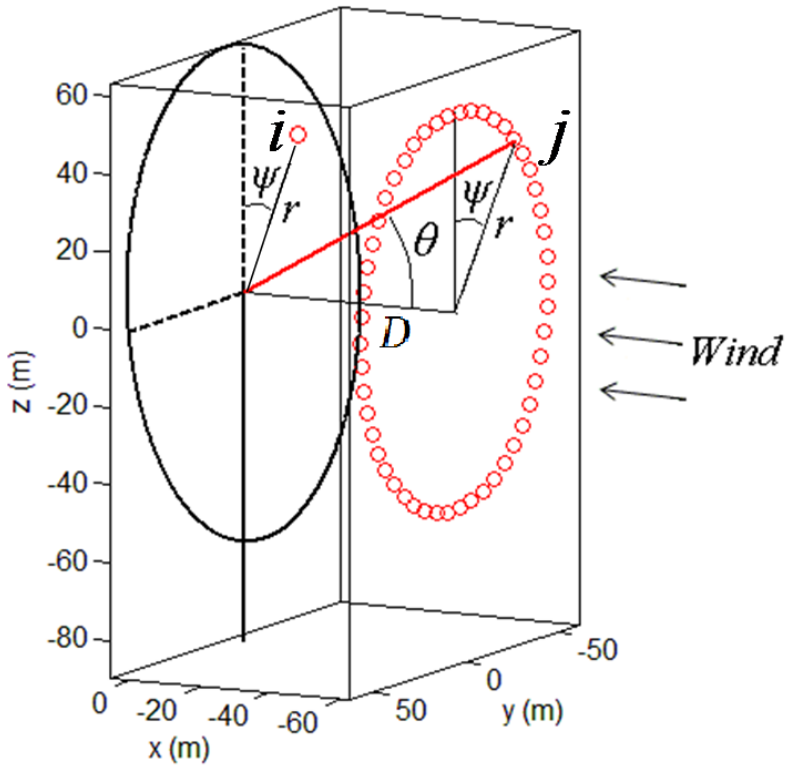

Figure 2. Coordinate system and measurement variables used. The LIDAR is assumed to be mounted in the wind turbine hub at (x_h, y_h, z_h) = (0, 0, 0).

The variable D represents the distance upwind, or in the longitudinal direction between the LIDAR and the measurement point. θ is the angle off of the longitudinal wind direction that the LIDAR is pointing. r is the radial distance from the longitudinal direction upwind of the LIDAR to the measurement point in the yz plane. In this figure, r is the radius of the scan pattern of a LIDAR measuring a circle upwind of the rotor. The dots represent where measurements would be taken for a LIDAR with a 50 hertz (Hz) sampling rate scanning at 60 revolutions per minute (rpm). This scenario will be discussed throughout the report. ψ is the azimuth angle of a LIDAR measurement in the yz plane. Point j indicates where a wind speed measurement is taken to estimate the wind that reaches point i after a delay time of D/U.

2.1 Range Weighting

Continuous-wave LIDAR determines the line-of-sight wind speed at a specific location by focusing the laser beam at that position in space. Rather than detecting the wind speed at only the intended point, a focal distance F away from the LIDAR, wind speed values along the entire laser beam are averaged according to what is called the "range weighting function," $W(F,R)$, to yield the detected value. The general effect of range weighting is the low-pass filtering of the true wind speed. As focal length increases, more high frequency wind information is lost in the measurement. The line-of-sight wind speed measurement, due to range weighting at a focal distance F, is given by:

$$u'_{LOS}(F) = \int_{-\infty}^{\infty} u_{LOS}(R) W(F,R) dR \qquad (0.1)$$

where

$u_{LOS}(R)$ = the line-of-sight velocity at a range R along the laser beam [13].

The range weighting function for a focal distance F is given by:

$$W(F,R) = \frac{K_N}{R^2 + \left(1 - \frac{R}{F}\right)^2 R_R^2} \tag{0.2}$$

where

R_R = the Rayleigh range
K_N = a normalizing constant
so that the entire range weighting function integrates to one.

For the commercially available Doppler LIDAR system modeled here [14], R_R is approximately 1,570 m.

The other leading technology for LIDAR wind speed measurements is pulsed LIDAR. Although pulsed LIDAR systems do not rely on focusing a laser at the range of interest as CW systems do, their spatial averaging can be similarly described by a range weighting function. Pulsed LIDARs emit a laser pulse and integrate the back-scattered light as the pulse travels through several "range gates." One drawback to using pulsed technology is that more time is required to integrate enough photons to provide a useful velocity estimate. In the remaining sections of this report, the focus will be on CW LIDAR for the measurement analyses.

Figure 3 (a) shows the normalized range weighting functions for the CW model at several focal distances, and the fixed weighting function for a pulsed model that is based on a commercially available LIDAR [14]. A previous analysis [8] has shown that the pulsed LIDAR causes roughly the same amount of measurement error as the CW LIDAR when it is focused at 135 m. The corresponding frequency responses of the weighting functions in terms of wavenumber k are shown in Figure 3 (b), where the low-pass filter behavior can be seen.

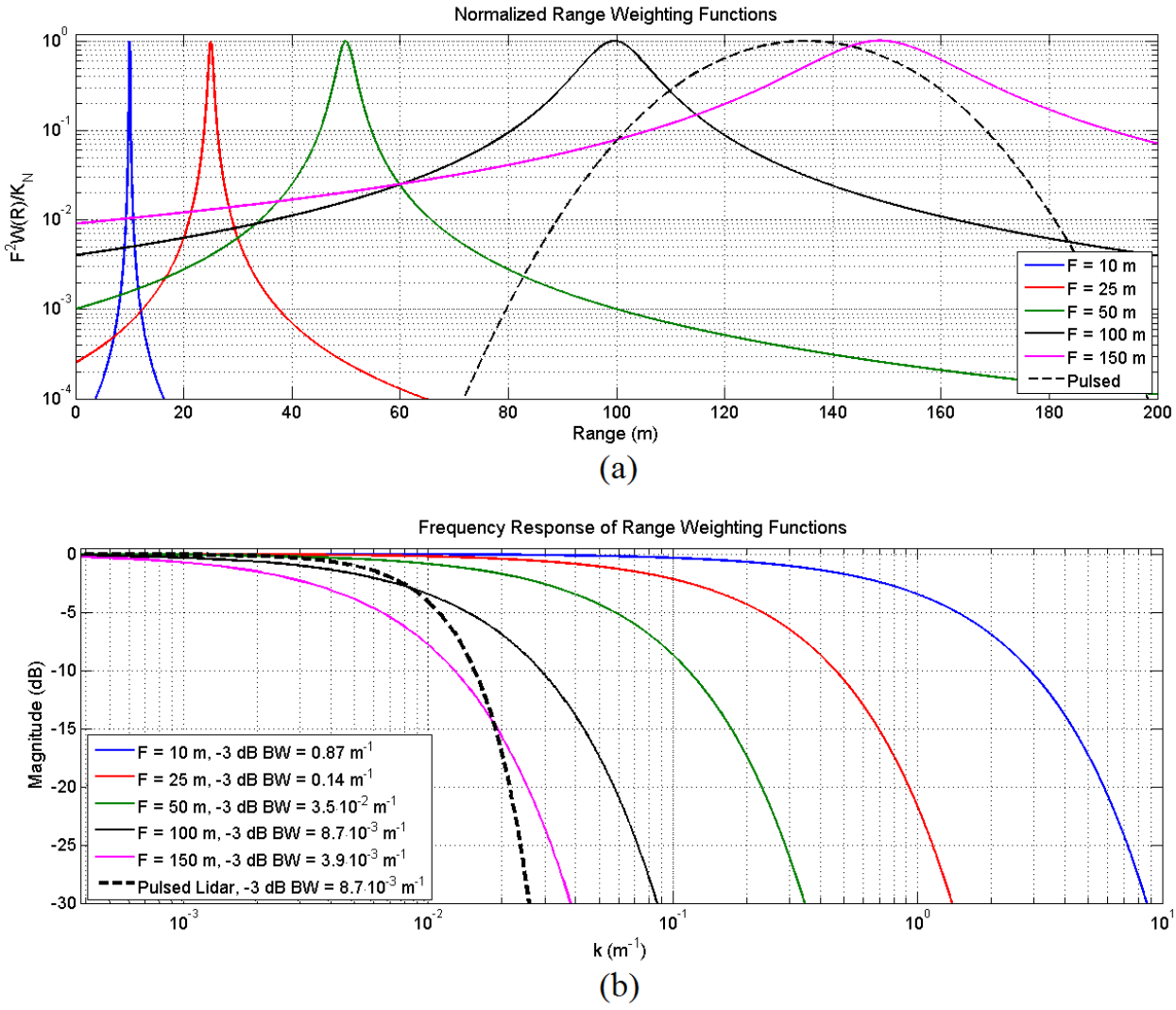

Figure 3. (a) Normalized range weighting functions, *W(F,R)*, for a continuous-wave LIDAR, which is representative of a commercially available model, at a variety of focal distances, *F*, and the fixed-range weighting function for the pulsed LIDAR. (b) Frequency responses of the normalized range weighting filters for a variety of focal distances along with the -3 decibel (dB) bandwidths of the filters.

2.2 Directional Bias

Since a single LIDAR measurement only provides a line-of-sight velocity, an estimate of the u component of the wind is formed by assuming $v = w = 0$, because ideally $u >> v,w$. The detected radial velocity when the LIDAR is aimed at an angle θ off of the x direction is given by [8]:

$$u_{LOS} = \sqrt{u^2 + v^2 + w^2}\cos(\phi) \tag{0.3}$$

where

φ = is the angle between the wind vector and the LIDAR direction.

Under the assumption that $v = w = 0$ ($\varphi = \theta$), the estimate of u is

$$\hat{u} = \frac{u_{LOS}}{\cos(\theta)}. \tag{0.4}$$

When the LIDAR is pointing nearly along the *x* axis, and θ is small, errors caused by the LIDAR geometry will be small because the measured radial velocity is dominated by the *u* component of wind speed. As θ increases, the radial velocity measured by the LIDAR will contain more contributions from the *v* and *w* components, thus causing higher error. An analysis of directional bias errors [8] has shown that, for a variable *u* velocity and a varying transverse wind speed component in the *yz* plane with magnitude $\sqrt{v^2 + w^2}$, and uniformly distributed random direction in the *yz* plane, the root mean square (RMS) measurement error is:

$$\sigma_{err} = \frac{\alpha_{\mathrm{RMS}} \tan\theta}{\sqrt{2}} \tag{0.5}$$

where

α_{RMS} = the RMS value of the transverse wind speed magnitude, or $\sqrt{\overline{v^2 + w^2}}$. The root mean square value of a signal is defined as the square root of the mean of the squared values of the signal.

2.3 LIDAR Performance in Frozen Wind Fields

Any *u* component estimate based on a LIDAR measurement in a frozen wind field will contain errors from both range weighting and directional bias as long as the measurement angle is non-zero. When the measurement angle is zero, only range weighting will contribute to measurement error. A previous study [8] examined measurement errors for a hub-mounted LIDAR that was scanning a circle of wind with radius *r* in front of the turbine as a function of preview distance *D* (see Figure 2). This scenario was motivated by the need for only one LIDAR, simplicity of implementation, and successful field testing [15]. For short preview distances *D*, the measurement angles θ tend to be very large, causing large directional bias errors that are proportional to tan (θ), as shown in Eq. 0.5. However, for large preview distances with smaller values of θ, range weighting from a CW LIDAR causes errors to be high. In the absence of wind evolution, it was found that a CW LIDAR has an optimal preview distance for each scan radius *r*, where the combined effects from range weighting and directional bias lead to a minimum achievable RMS error.

A summary of the error-versus-preview-distance study is provided in Figure 4, for *r* = 50%, 75%, and 100% blade span for the 5-MW model turbine (31.5, 47.25, and 63 m, respectively). Results are shown for the CW and pulsed models using an unstable Great Plains-Low Level Jet wind condition, as described in Section 4 (Table 1). For CW LIDAR, the minimum-error preview distance is roughly 115 m for *r* = 50% blade span, just under 150 m for *r* = 75% blade span, and over 200 m for *r* = 100% blade span. Note that for pulsed LIDAR, there is no minimum-error preview distance in the absence of wind evolution because the range weighting function remains the same as the preview distance increases. A goal of the research presented in this report is to provide more accurate error-versus-preview-distance curves by introducing the effects of wind evolution, as described by longitudinal coherence loss which is discussed in the next section.

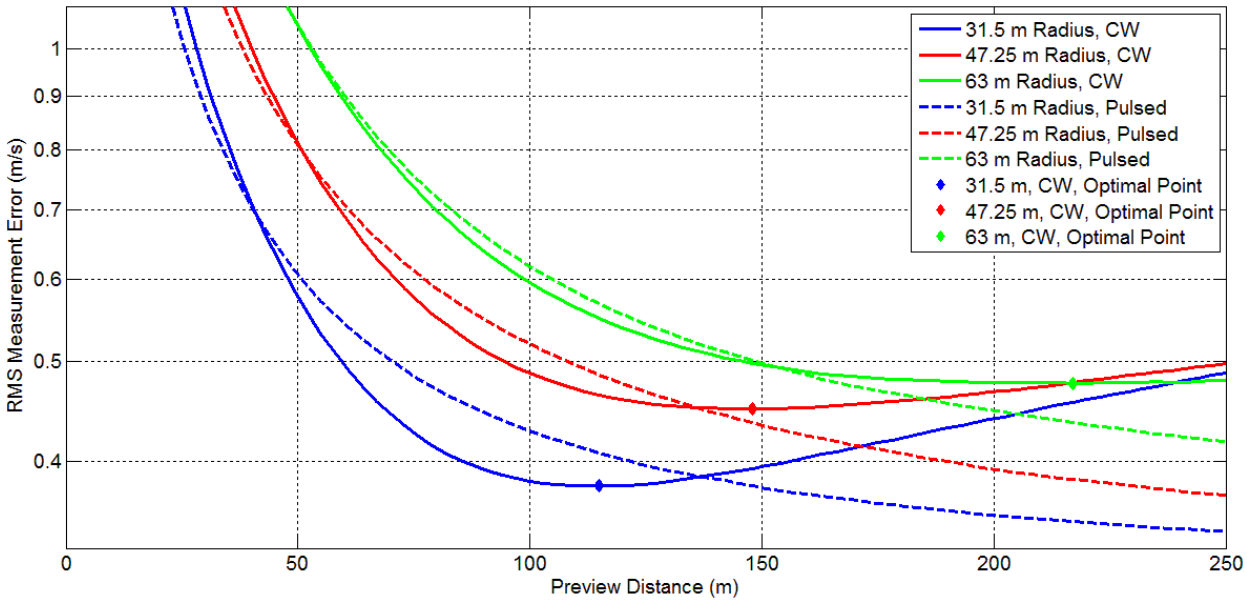

Figure 4. RMS measurement error as a function of preview distance for the 5-MW turbine model in a wind field that was generated using TurbSim, with parameters given in Table 1. Results are shown for CW and pulsed LIDARs scanning at radii of 50%, 75%, and 100% blade span [blade span for the 5-MW turbine is 63 meters (m)].

3 Coherence in Wind Fields

3.1 Coherence

The degree to which wind speeds, at any two points in a wind field, are correlated is given by a coherence function. Coherence will vary depending on the spatial separation of the two points of interest. Wind fields used in a previous study of Light Detection and Ranging (LIDAR) system performance [8] included coherence between wind speeds that were separated in the transverse *yz* plane, or the plane that was perpendicular to the wind direction. However, using Taylor's hypothesis, wind speeds at points that are separated in the longitudinal, or mean wind direction, are always perfectly correlated. In this section, the researchers describe the coherence between wind speeds at any two points in a wind field, including wind evolution. In this report, the specific type of coherence analyzed is magnitude-squared coherence, which is a function of frequency, where a value of one indicates that the wind is perfectly correlated at the two locations and a value of zero indicates that the wind is completely uncorrelated at the two locations. In addition to magnitude, the phase information for wind at the two locations can be used to assess the degree of wind evolution. Under Taylor's frozen turbulence hypothesis, the coherence magnitude would be one for all frequencies, and the phase would be $2\pi D/\lambda$ for two points that are longitudinally separated by a distance D, where λ is the wavelength of the turbulent eddies in the flow at the frequency f, given by the relationship $\lambda=U/f$.

Magnitude-squared coherence, often notated as γ^2, is defined as:

$$\gamma_{xy}^2 = \frac{|S_{xy}|^2}{S_{xx}S_{yy}} \tag{3.1}$$

where

S_{xy} = the cross-power spectral density (CPSD) between signals x and y
S_{xx} = the power spectral density (PSD) of signal x.

CPSD is given by:

$$S_{xy} = F\{R_{xy}(\tau)\} \tag{3.2}$$

where

$F\{\cdot\}$ = the Fourier transform

and the cross-correlation function $R_{xy}(\tau)$ is defined as:

$$R_{xy}(\tau) = \int_{-\infty}^{\infty} x(t)y^*(t+\tau)dt \tag{3.3}$$

where

$\{\}^*$ = the complex conjugate.

The phase associated with coherence is given by

$$\varphi_{xy}(f) = \text{angle}(S_{xy}(f)). \tag{3.4}$$

3.2 Correlation Between Points in a Wind Field

To describe the correlation between all points in a wind field with three spatial dimensions, a coherence function must exist for each pair of points. For a wind field with two spatial dimensions, as illustrated in Figure 5, each wind speed location must be correlated with each other location in the longitudinal, transverse (vertical in this example), and diagonal directions. In Section 4, the two different wind evolution scenarios are described. The first scenario involves introducing wind evolution to a frozen wind field using a simple analytic formula for longitudinal coherence. Transverse coherence functions for separations in the *yz* plane are already defined for the wind field and longitudinal coherence must be introduced, but there is some ambiguity in the correlation between points that are separated diagonally, or with some combination of transverse and longitudinal separation. The second scenario involves using a large eddy simulation (LES) wind field to calculate coherence functions for both transverse and longitudinal separations.

When introducing wind evolution to a frozen wind field, the diagonal coherence functions must be defined. A range of possibilities exist, but a simple solution is to restrict the diagonal coherence functions to be the product of the coherence resulting from the transverse separation and the coherence resulting from the longitudinal separation. This form of diagonal coherence is illustrated in Figure 5 and is the coherence that would result if the wind speeds at points x_1,z_1 and x_1,z_2 were correlated independently from the wind speeds at points x_1,z_2 and x_3,z_2. Evaluations of diagonal coherence functions in the LES wind field show that this assumption is very accurate for short longitudinal separations (below ~30 m), and is a lower bound on the true diagonal coherence.

For wind fields with three spatial dimensions, nine coherence functions exist to describe the correlation between wind speeds at two different points. Each of the *u*, *v*, and *w* components at one point are correlated with each component at the other point. For the Great Plains-Low Level Jet wind field that was used in this report, all of the coherence functions were non-zero, which will be discussed more in Section 4. In general, the correlations between the *u* components, the *v* components, and the *w* components at both points are greater than the "cross" component correlations.

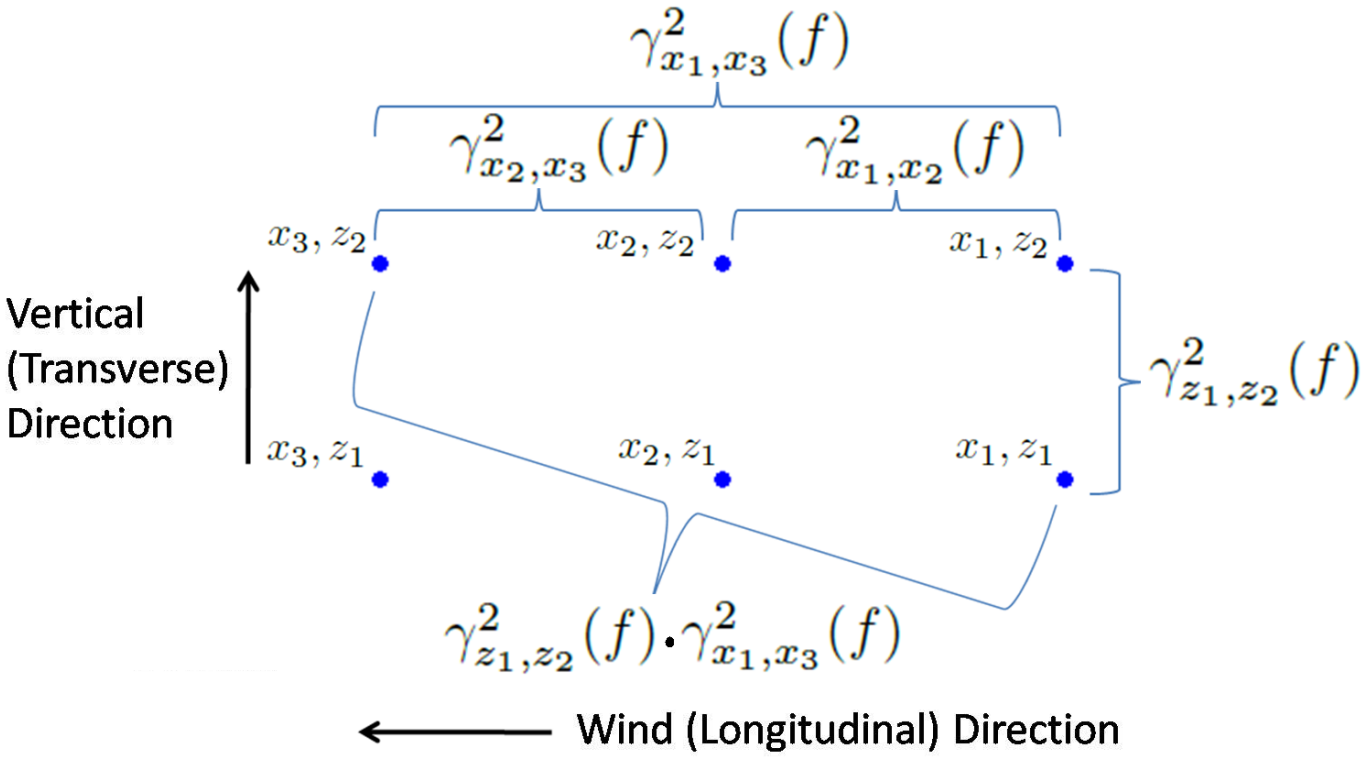

Figure 5. Longitudinal, transverse, and diagonal correlations between wind speed locations in a wind field with two spatial dimensions

4 Wind Fields and Wind Evolution Models

Analyses of Light Detection and Ranging (LIDAR) system measurement coherence are performed for two types of wind fields. A wind field characteristic of the U.S. Great Plains region generated by TurbSim is used to demonstrate the addition of wind evolution to a frozen wind field. A simple exponential form of longitudinal coherence is used to create wind evolution in this wind field. By adjusting a decay parameter, the intensity of wind evolution can be varied. The second wind field analyzed is a large eddy simulation (LES) of a stable boundary layer. All statistics used to calculate measurement coherence for this wind field are based on measurements from the LES wind field.

4.1 The Great Plains-Low Level Jet Wind Field

Wind conditions generated by TurbSim using the Great Plains-Low Level Jet (GP_LLJ) spectral model [10] were used in previous studies [6, 8, 16] to evaluate LIDAR measurements and controller performance. The wind fields are designed to be used with the National Renewable Energy Laboratory's (NREL's) 5-megawatt (MW) turbine model with a hub height of 90 meters (m) and a rotor radius of 63 m. One of these conditions was chosen as a wind field to which wind evolution can be introduced. Table 1 summarizes this unstable wind condition at three different heights, including hub height and 50 meters below and above hub height.

Table 1. A Summary of the Unstable Great Plains-Low Level Jet Wind Field Used for Wind Speed Measurement Analysis with the 5-Megawatt (MW) Wind Turbine Model

Height (m)	U (m/s)	u^* (m/s)	TI_U (%)	TI_V (%)	TI_W (%)
40	12.25	0.598	9.2	9.4	7.2
90	13	0.530	6.6	7.1	5.7
140	13.44	0.425	4.6	5.3	4.4

Notes: The turbine layer gradient Richardson number is Ri_{TL} = -0.1. Wind shear is defined using a power law with exponent α_D = 0.077. U indicates the mean streamwise wind speed and u^* is the height-dependent friction velocity. Friction velocity is defined as $\boldsymbol{u}^* = \sqrt{|\overline{\boldsymbol{u'w'}}|}$, where $u' = u - \overline{u}$ and $w' = w - \overline{w}$. TI_U, TI_V, and TI_W are the turbulence intensities of the u, v, and w components of wind speed.

The spectra of the u, v, and w components of wind speed are shown in Figure 6 for the heights summarized in Table 1. The spectra are included to illustrate some of the trends that can be seen in the measurement coherence results (described in Section 6).

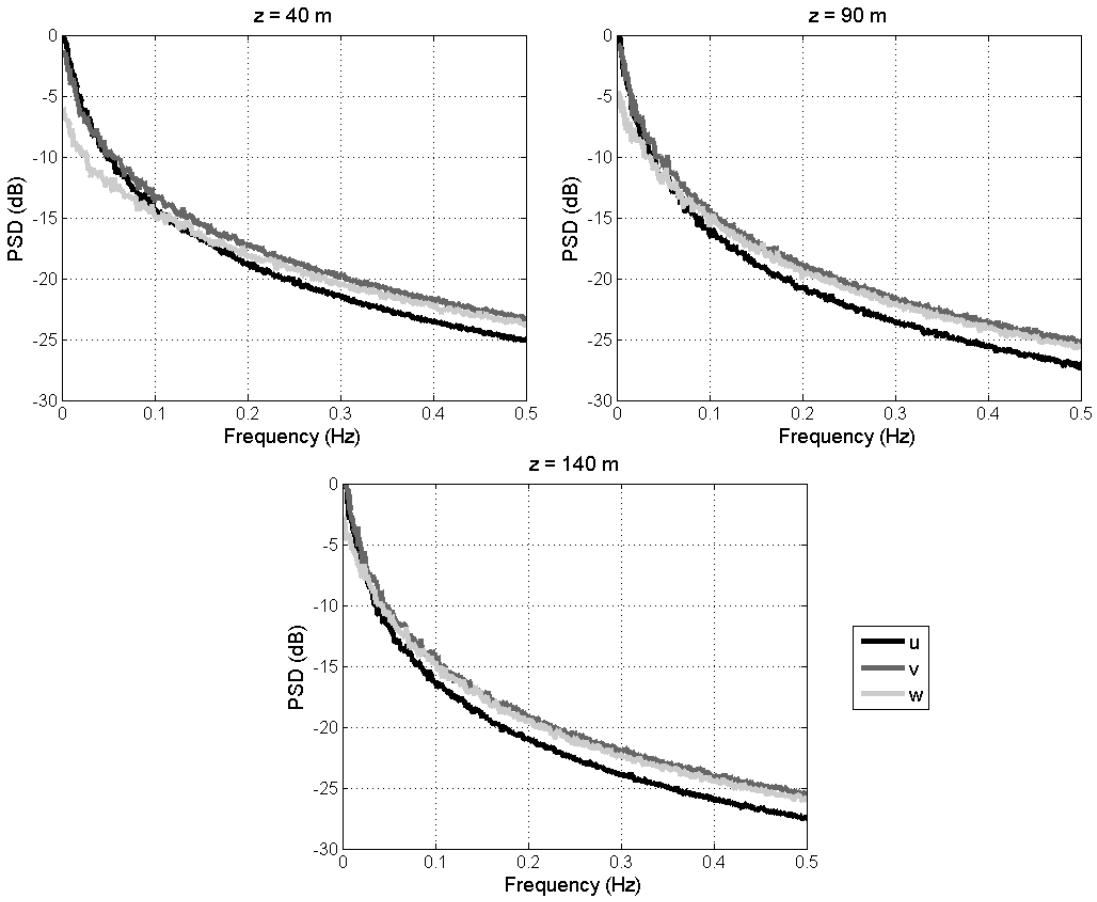

Figure 6. Power spectral densities of wind speed components at heights of 40 m, 90 m, and 140 m for the Great Plains-Low Level Jet wind condition (described in Table 1)

For TurbSim's Great Plains-Low Level Jet spectral model, the transverse coherence at a frequency f between points i and j in the yz plane is defined as:

$$\gamma_{i,j}^2(f,l) = \exp\left(-2\alpha_l\sqrt{\left(\frac{f r_{i,j}}{\bar{u}_{i,j}}\right)^2 + \left(b_l r_{i,j}\right)^2}\right), \tag{4.1}$$

where

$r_{i,j}$ = the distance between the points
$\bar{u}_{i,j}$ = the average of the wind speeds at the two points
a_l and b_l are coherence parameters defined for the u, v, and w wind components ($l \in \{u, v, w\}$) [10].

The coherence parameters a_l and b_l are based on field measurements and are $a_u = 9.513$, $a_v = 6.291$, and $a_w = 4.535$ and $b_u = 0.384 \cdot 10^{-3}$, $b_v = 0.108 \cdot 10^{-2}$, and $b_w = 0.209 \cdot 10^{-2}$. The u component of transverse coherence given by Eq. 4.1 is shown in Figure 7 (a) for transverse separations in the y direction of 2, 4, 8, 16, and 32 m at hub height (z = 90 m). This range of

distances is indicative of the transverse separations used in calculations of measurement coherence and is described in the next section.

As mentioned in the previous section, the coherence between the *u* and *v*, *u* and *w*, and *v* and *w* components of wind speed is non-zero for the Great Plains-Low Level Jet wind field that was created using TurbSim. The average Reynolds stress [10] *u'w'* for this wind field, where $u' = u - \bar{u}$ and $w' = w - \bar{w}$, is -0.281 at hub height, results in non-zero *uw* coherence functions. For the *u* and *v* components, the average Reynolds stress *u'v'* is ±0.277 at hub height, where the sign varies with each 10-minute realization of the wind condition. Furthermore, because of the negative sign of the average *u'w'* Reynolds stress, the phase of the *uw* coherence function, given by Eq. 3.4, is 180°. For consistency, the sign of the *uv* correlation is being treated as positive. Although the *v* and *w* components are correlated as well, the LIDAR measurement scenarios that are investigated in this report include either *u* and *v* components or *u* and *w* components, but not both simultaneously. Therefore, the *vw* correlations are not used in any calculations. Figure 7 (b) contains the *uw* coherence curves for three heights, corresponding to the bottom of the rotor, hub height, and the top of the rotor, as well as the *uv* coherence function at hub height.

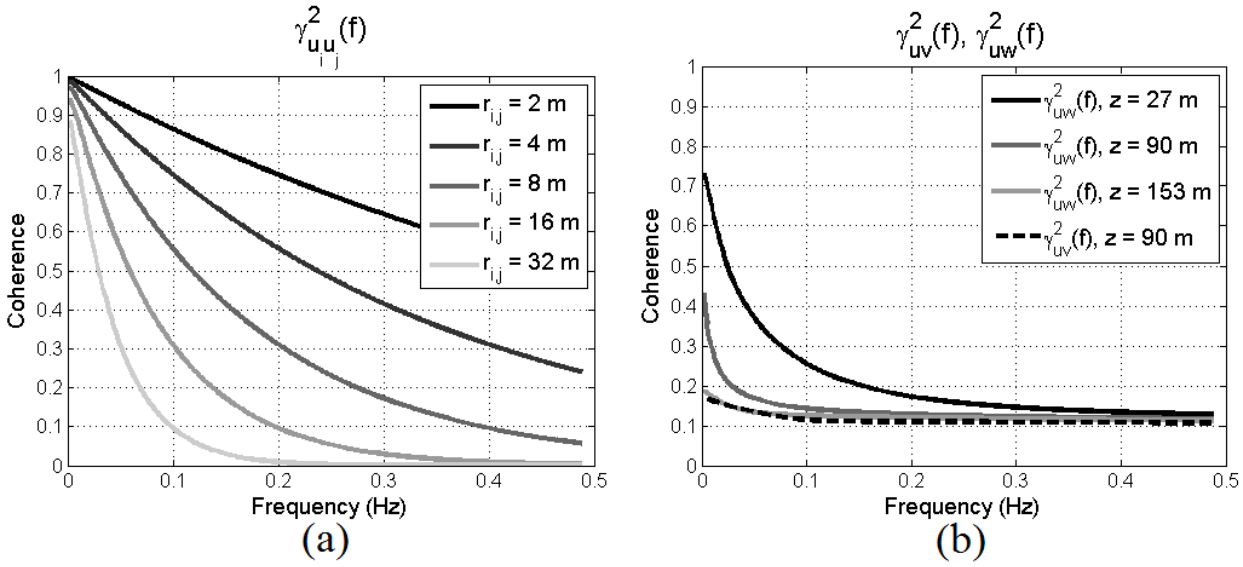

Figure 7. Coherence summary for the Great Plains-Low Level Jet wind condition. (a) Transverse coherence functions for the *u* component at a height of *z* = 90 m for transverse separations of 2, 4, 8, 16, and 32 m. (b) Coherence between the *u* and *w* components of wind at *z* = 27 m, 90 m, and 153 m, which correspond to the bottom of the rotor, the hub height, and the top of the rotor, and coherence between the *u* and *v* components at *z* = 90 m.

4.2 Exponential Wind Evolution Model

A model of wind evolution can be formed using a simple exponential model of coherence that is a function of the non-dimensional product between the eddy wavenumber and longitudinal separation, as suggested in Pielke and Panofsky [17]. This model is given by:

$$\gamma^2(kD) = e^{-akD} \tag{4.2}$$

where

k = the eddy wavenumber ($k = f/U$)
D = the longitudinal separation between points in the wind field
a = a dimensionless decay parameter.

This simple exponential model allows for an easy method of varying the amount of wind evolution by adjusting the decay parameter. Increasing a exaggerates the effects of wind evolution by causing the coherence curve to decay faster with frequency. In Section 6, LIDAR measurement coherence is calculated for the Great Plains-Low Level Jet wind field using this exponential longitudinal coherence function to describe the evolution of the u, v, and w components for a range of decay parameters. Although it is difficult to directly compare different wind evolution models, decay parameters between 0.3 and 0.6 in this unstable flow seem to produce roughly the same measurement coherence as the weakly stable LES wind field.

4.3 LES Stable Boundary Layer Wind Field

A large eddy simulation of a stable boundary layer [11], provided by the National Center for Atmospheric Research (NCAR), is used to calculate longitudinal coherence curves to model wind evolution. The data is sampled at a rate of roughly 1 hertz (Hz), so the bandwidth used for all of the spectral results in this report is approximately 0.5 Hz. The 13-minute LES wind field spans 1,000 m in the x and y directions, with data existing for heights between 50 and 150 m. The spatial resolution is 2 m in the x and y directions and 1 m in the z direction. A summary of the wind field at heights of 50 m, 100 m, and 150 m is provided in Table 2. The spectra of the u, v, and w components of wind speed are shown in Figure 8 for the heights summarized in Table 2.

Table 2. A Summary of the Stable Large Eddy Simulation Wind Field Provided by the National Center for Atmospheric Research, with a Monin-Obukhov Stability Parameter of zi/L = 2

Height (m)	U (m/s)	TI_U (%)	TI_V (%)	TI_W (%)
50	5.7	6.8	5.8	4.4
100	7.6	3.7	3.3	2.4
150	9.1	1.9	2.0	1.23

Note: U indicates the mean streamwise wind speed and TI_U, TI_V, and TI_W are the turbulence intensities of the u, v, and w components of wind speed.

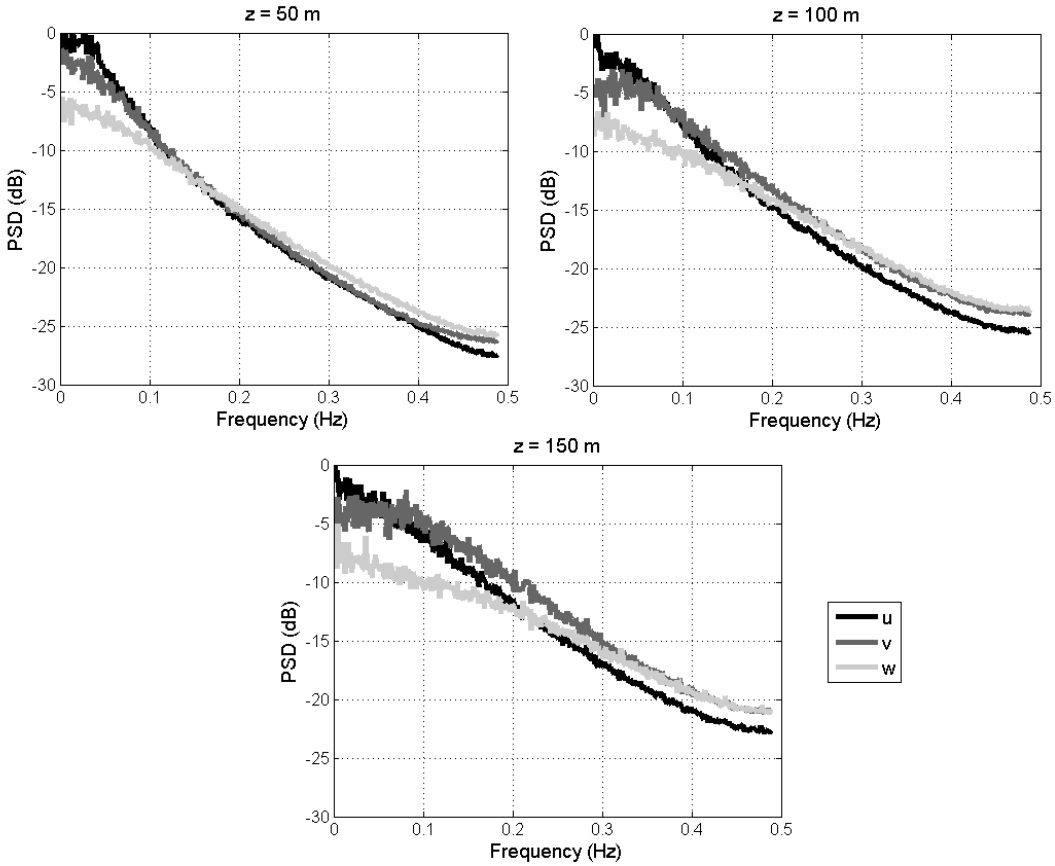

Figure 8. Power spectral densities of wind speed components at heights of 50 m, 100 m, and 150 m for the stable large eddy simulation wind field described in Table 2

Transverse coherence curves for separations in the *y* and *z* directions for the *u* component derived from the LES wind field are shown in Figure 9 for transverse separations of 1, 2, 4, 8, and 16 m. This range of separations is typical of transverse distances used in the calculations in Section 6. Coherence curves were measured in the *y* direction at a height of 100 m and in the *z* direction at all heights. Since there is a small but noticeable difference between coherence curves in the *z* direction at different heights, the coherence curves in the lower half of the wind field are used to calculate average coherence curves for heights between 50 m and 100 m. Likewise, the coherences in the upper half of the wind field are averaged to produce a single family of coherence curves for heights between 100 m and 150 m. Coherence in the *z* direction is much lower than in the *y* direction, likely due to stable stratification in the wind field. Because the coherence curves for the *u*, *v*, and *w* components are similar, the *u* component coherences are used to describe all three components in this report.

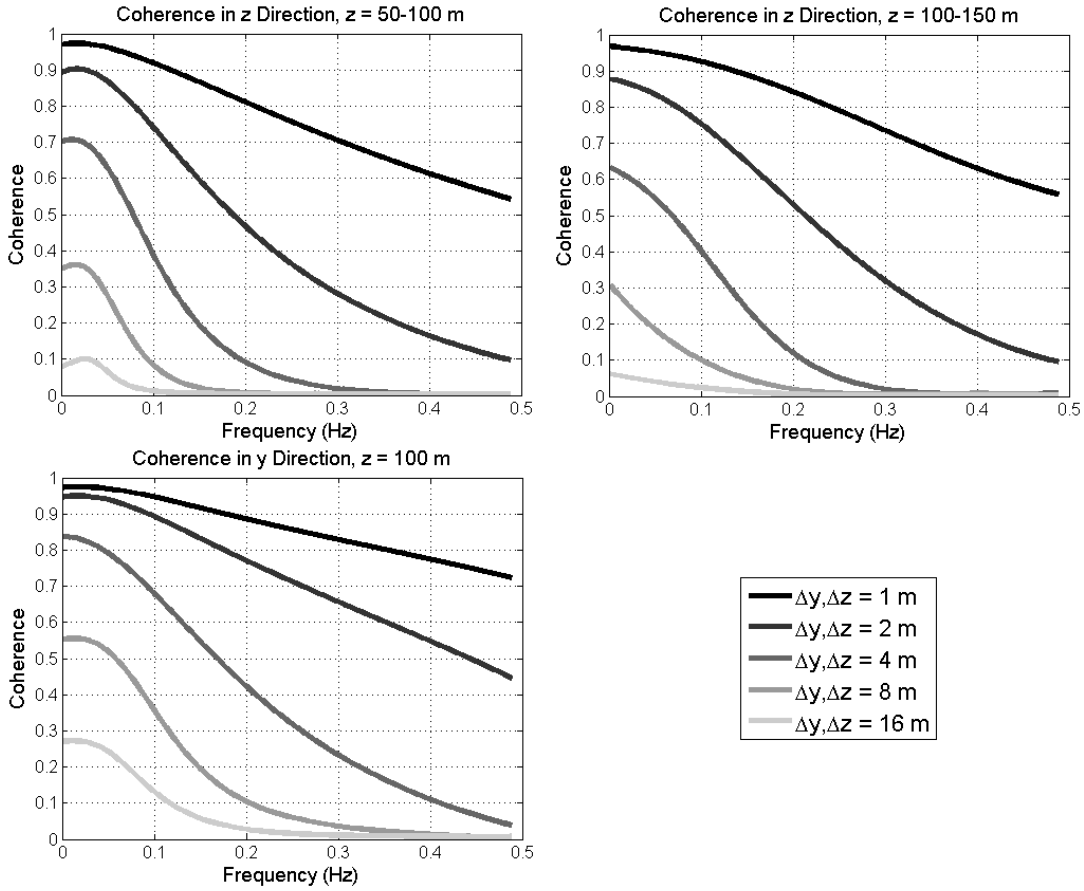

Figure 9. Transverse coherence curves for the stable LES wind field measured in the *y* direction at a height of 100 m, and average coherence curves in the *z* direction based on measurements at heights between 50 and 100 m and 100 and 150 m

Because of wind shear, wind evolution as a function of the longitudinal separation between points varies with height. In general, as the mean streamwise wind speed increases, the coherence curves for a given longitudinal separation increase, because the time that elapses as wind travels the same distance decreases. Figure 10 contains longitudinal coherence curves for the *u* component based on measurements at a height of 100 m for longitudinal separations of 10, 25, 50, 100, and 200 m. The measurement scenarios examined in Section 6 include preview distances of up to 200 m. Because of wind shear, coherence curves for heights above 100 m are generally higher for a given frequency while curves for heights below 100 m are lower. As a simplification, the coherence curves for the *u* component are determined at the height of 100 m and are used to describe wind evolution for all components at all heights.

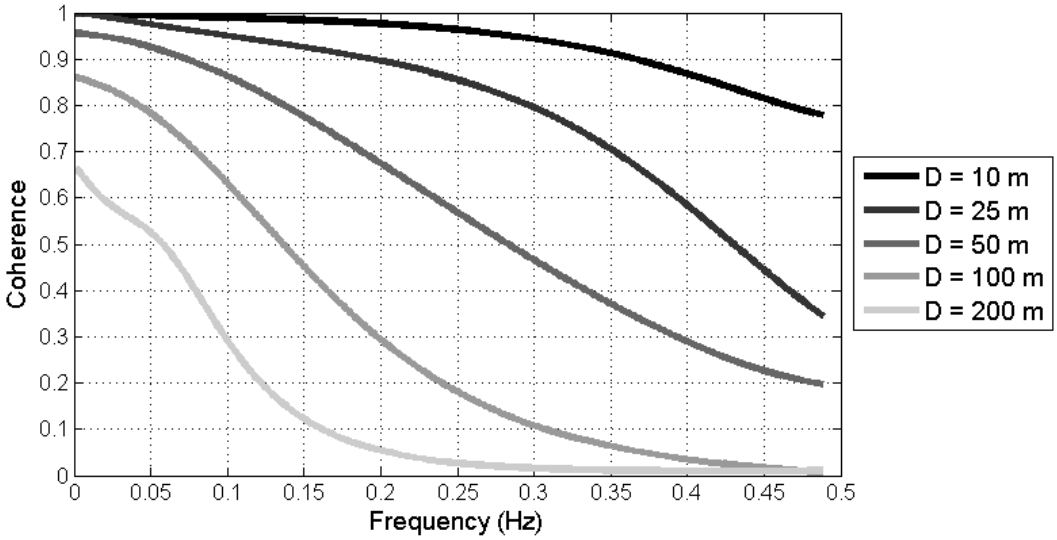

Figure 10. Longitudinal coherence curves for the stable LES wind field based on measurements at a height of 100 m

5 LIDAR Measurement Coherence

The quality of a wind speed measurement as influenced by evolution can be judged by the coherence between the estimate of the *u* component of the line-of-sight Light Detection and Ranging (LIDAR) system measurement and the true *u* component that reaches the rotor plane. Referring to Figure 2, the upwind point at which the LIDAR is focused is called point *j*, while the point where the evolved wind meets the rotor plane is called point *i*. Points *i* and *j* have the same transverse coordinates in the *yz* plane but are separated longitudinally by the preview distance *D*. The coherence between the estimate of the *u* component at point *j* and the true *u* component at point *i* is written as:

$$\gamma^2_{u_i\hat{u}'_j}(f) = \frac{\left|S_{u_i\hat{u}'_j}(f)\right|^2}{S_{u_iu_i(f)}S_{\hat{u}'_j\hat{u}'_j}(f)} \tag{5.1}$$

where

$\hat{u}'_j$ = the estimate of the *u* component based on the line-of-sight LIDAR measurement.

The following derivation of the measurement coherence yields a formula in terms of power spectral densities of the wind and coherence functions for any pair of points in the wind field, which are assumed as known quantities and are based on the wind field description in Section 4. This derivation is based on an analysis given by Schlipf, for the simple case where there is neither range weighting nor wind evolution [18]. While measurement coherence can be estimated by simulating LIDAR measurements in an evolving wind field, the formulas outlined in this section provide the exact coherence values. An advantage of using formulas to calculate measurement coherence is that direct calculations of coherence using spectral properties of the wind field are much less computationally expensive than time-domain simulations of LIDAR measurements. In addition, properties of the wind field can be easily varied without generating additional four-dimensional wind fields.

If the unit vector is represented in the direction that the LIDAR is pointing as

$$\vec{l} = [l_x, l_y, l_z] \tag{5.2}$$

then, based on the coordinate system in Figure 2, the line-of-sight wind speed measurement is

$$u_{j,LOS} = l_x u_j - l_y v_j - l_z w_j. \tag{5.3}$$

Furthermore, the range weighted line-of-sight measurement is represented as:

$$u'_{j,LOS} = l_x u'_j - l_y v'_j - l_z w'_j \tag{5.4}$$

where

the range weighted velocity vector is given by

$$\vec{u}'_j = \int_0^\infty \vec{u}(R\vec{l})W(F,R)dR \tag{5.5}$$

with

$$\vec{u} = [u, v, w]. \tag{5.6}$$

Based on equations (Eqs.) 5.3 and 5.4, the estimate of the *u* component of a line-of-sight point measurement is given by

$$\begin{aligned}\hat{u}_j &= \frac{1}{l_x}u_{j,LOS} \\ &= u_j - \frac{l_y}{l_x}v_j - \frac{l_z}{l_x}w_j\end{aligned} \tag{5.7}$$

and the estimate of *u* for a line-of-sight range weighted measurement is given by

$$\begin{aligned}\hat{u}'_j &= \frac{1}{l_x}u'_{j,LOS} \\ &= u'_j - \frac{l_y}{l_x}v'_j - \frac{l_z}{l_x}w'_j.\end{aligned} \tag{5.8}$$

Note that forming an estimate of the *u* component in Eqs. 5.7 and 5.8, by dividing the line-of-sight velocity by l_x, is equivalent to dividing the line-of-sight velocity by cos(θ) in Eq. 0.4. The measurement angle θ is equivalent to $\tan^{-1}\left(\frac{\sqrt{l_y^2+l_z^2}}{l_x}\right)$.

Using Eqs. 5.2 through 5.8, the terms $S_{\hat{u}'_j\hat{u}'_j}(f)$ and $S_{u_i\hat{u}'_j}(f)$ from Eq. 5.1 can be written in terms of the transverse and longitudinal coherence functions in the wind field and the power spectral density functions of the wind speeds. Letting $\widehat{U}(f) = F\{\hat{u}(t)\}$ and $\{\cdot\}^*$ represent the complex conjugate operation, the $S_{\hat{u}'_j\hat{u}'_j}(f)$ term can be expanded as:

$$\begin{aligned}S_{\hat{u}'_j\hat{u}'_j}(f) &= \overline{\widehat{U}'_j(f)\widehat{U}'^*_j(f)} \\ &= \overline{\left(\int_0^\infty W(F,\alpha)\widehat{U}(\alpha\vec{l},f)d\alpha\right)\left(\int_0^\infty W(F,\beta)\widehat{U}^*(\beta\vec{l},f)d\beta\right)} \\ &= \int_0^\infty\int_0^\infty W(F,\alpha)W(F,\beta)\,\overline{\widehat{U}(\alpha\vec{l},f)\widehat{U}^*(\beta\vec{l},f)}d\alpha\,d\beta \\ &= \int_0^\infty\int_0^\infty W(F,\alpha)W(F,\beta)S_{\hat{u}_{\alpha\vec{l}}\hat{u}_{\beta\vec{l}}}(f)\,d\alpha\,d\beta\end{aligned} \tag{5.9}$$

where

$S_{\hat{u}_{\alpha\vec{l}}\hat{u}_{\beta\vec{l}}}(f)$ = the cross-power spectral density (CPSD) between the estimates of the *u* components at points with distances α and β along the LIDAR beam. For each α, β pair, $S_{\hat{u}_{\alpha\vec{l}}\hat{u}_{\beta\vec{l}}}(f)$ can be expanded as

$$S_{\hat{u}_{\alpha\vec{l}}\hat{u}_{\beta\vec{l}}}(f) = \overline{\widehat{U}_{\alpha\vec{l}}(f)\widehat{U}^*_{\beta\vec{l}}(f)}$$

$$= \overline{\left(U_{\alpha\vec{l}}(f) - \frac{l_y}{l_x}V_{\alpha\vec{l}}(f) - \frac{l_z}{l_x}W_{\alpha\vec{l}}(f)\right)\left(U^*_{\beta\vec{l}}(f) - \frac{l_y}{l_x}V^*_{\beta\vec{l}}(f) - \frac{l_z}{l_x}W^*_{\beta\vec{l}}(f)\right)}$$

$$= S_{u_{\alpha\vec{l}}u_{\beta\vec{l}}}(f) + \left(\frac{l_y}{l_x}\right)^2 S_{v_{\alpha\vec{l}}v_{\beta\vec{l}}}(f) + \left(\frac{l_z}{l_x}\right)^2 S_{w_{\alpha\vec{l}}w_{\beta\vec{l}}}(f)$$
$$- \frac{l_y}{l_x}\left(S_{u_{\alpha\vec{l}}v_{\beta\vec{l}}}(f) + S_{v_{\alpha\vec{l}}u_{\beta\vec{l}}}(f)\right) - \frac{l_z}{l_x}\left(S_{u_{\alpha\vec{l}}w_{\beta\vec{l}}}(f) + S_{w_{\alpha\vec{l}}u_{\beta\vec{l}}}(f)\right)$$
$$+ \frac{l_y l_z}{l_x^2}\left(S_{v_{\alpha\vec{l}}w_{\beta\vec{l}}}(f) + S_{w_{\alpha\vec{l}}v_{\beta\vec{l}}}(f)\right). \quad (5.10)$$

The measurement scenarios discussed in this report include azimuth angles of $\psi = 0°$, $\psi = 90°$, $\psi = 180°$, and $\psi = -90°$. As a result, the unit vector in the LIDAR direction either contains $l_y = 0$ or $l_z = 0$. In this case, Eq. 5.10 simplifies to

$$S_{\hat{u}_{\alpha\vec{l}}\hat{u}_{\beta\vec{l}}}(f) = S_{u_{\alpha\vec{l}}u_{\beta\vec{l}}}(f) + \left(\frac{l_y}{l_x}\right)^2 S_{v_{\alpha\vec{l}}v_{\beta\vec{l}}}(f) + \left(\frac{l_z}{l_x}\right)^2 S_{w_{\alpha\vec{l}}w_{\beta\vec{l}}}(f)$$
$$- \frac{l_y}{l_x}\left(S_{u_{\alpha\vec{l}}v_{\beta\vec{l}}}(f) + S_{v_{\alpha\vec{l}}u_{\beta\vec{l}}}(f)\right) - \frac{l_z}{l_x}\left(S_{u_{\alpha\vec{l}}w_{\beta\vec{l}}}(f) + S_{w_{\alpha\vec{l}}u_{\beta\vec{l}}}(f)\right). \quad (5.11)$$

The complex-valued CPSD in Eq. 5.11 can be written in terms of its magnitude and phase as

$$S_{\hat{u}_{\alpha\vec{l}}\hat{u}_{\beta\vec{l}}}(f) = \left|S_{\hat{u}_{\alpha\vec{l}}\hat{u}_{\beta\vec{l}}}(f)\right| e^{j\varphi_{\alpha\vec{l}\,\beta\vec{l}}(f)}. \quad (5.12)$$

Each term in Eq. 5.11 has the same phase, which is given by:

$$\varphi_{\alpha\vec{l}\,\beta\vec{l}}(f) = \frac{D_{\alpha\vec{l}\,\beta\vec{l}}f}{\bar{U}} \quad (5.13)$$

where

$D_{\alpha\vec{l}\,\beta\vec{l}}$ is the longitudinal separation between points at distances α and β along the LIDAR beam.

With knowledge of the power spectral densities (PSDs) of the wind field and the coherence between wind at any two points in the wind field, the magnitudes of the CPSDs can be found by rearranging the formula for coherence in Eq. 3.1 as

$$\left|S_{xy}\right| = \sqrt{S_{xx}S_{yy}\gamma^2_{xy}}. \quad (5.14)$$

The calculation of the $S_{u_i\hat{u}'_j}(f)$ term from Eq. 5.1 is performed in a similar fashion as the $S_{\hat{u}'_j\hat{u}'_j}(f)$ term. $S_{u_i\hat{u}'_j}(f)$ can be expanded as:

$$S_{u_i\hat{u}'_j}(f) = \overline{U_\iota(f)\hat{U}'^*_j(f)}$$

$$= \overline{U_i(f)\left(\int_0^\infty W(F,\beta)\widehat{U}^*\left(R\vec{l},f\right)dR\right)}$$
$$= \int_0^\infty W(F,R)\overline{U_i\left(\alpha\vec{l},f\right)\widehat{U}^*\left(R\vec{l},f\right)}\,dR$$
$$= \int_0^\infty W(F,R)S_{u_i\widehat{u}_{R\vec{l}}}(f)\,dR \tag{5.15}$$

where

$S_{u_i\widehat{u}_{R\vec{l}}}(f)$ = the CPSD between the *u* component at point *i* on the rotor plane

the *u* estimate is based on the line-of-sight point measurement at a distance *R* along the LIDAR beam.

For each distance *R*, $S_{u_i\widehat{u}_{R\vec{l}}}(f)$ can be expanded as

$$S_{u_i\widehat{u}_{R\vec{l}}}(f) = \overline{U_i(f)\widehat{U}^*_{R\vec{l}}(f)}$$
$$= \overline{U_i(f)\left(U^*_{R\vec{l}}(f) - \frac{l_y}{l_x}V^*_{R\vec{l}}(f) - \frac{l_z}{l_x}W^*_{R\vec{l}}(f)\right)}$$
$$= S_{u_iu_{R\vec{l}}}(f) - \frac{l_y}{l_x}S_{u_iv_{R\vec{l}}}(f) - \frac{l_z}{l_x}S_{u_iw_{R\vec{l}}}(f). \tag{5.16}$$

Once again, Eq. 5.16 can be described by its magnitude and phase as:

$$S_{u_iu_{R\vec{l}}}(f) = \left|S_{u_iu_{R\vec{l}}}(f)\right| e^{j\varphi_{i\,R\vec{l}}(f)} \tag{5.17}$$

where

$$\varphi_{i\,R\vec{l}}(f) = \frac{D_{i\,R\vec{l}}f}{\bar{U}} \tag{5.18}$$

with $D_{i\,R\vec{l}}$ representing the longitudinal separation between the point *i* on the rotor plane and the distance *R* along the LIDAR beam.

5.1 Components of Measurement Coherence

There are several factors that may cause a decrease in measurement coherence as defined by Eq. 5.1. In addition to wind evolution, error sources that are characteristic of LIDAR measurements in non-evolving wind fields, such as range weighting and directional bias, will cause a loss of coherence. Figure 11 and Figure 12 compare the components of coherence for three different measurement geometries by showing the measurement coherence that was calculated using Eqs. 5.1 through 5.18, with various combinations of the error sources included. Figure 11 uses the spectral properties of the TurbSim wind field with exponential wind evolution, while Figure 12 uses characteristics of the large eddy simulation (LES) wind field. The decay parameter used with the exponential model is $a = 0.45$. Coherence plots for both wind fields are provided to compare and contrast the simple wind evolution model and the model that is derived from the LES results. In both figures, each scenario involves a LIDAR that is located at the hub, measuring wind at a radial distance of $r = 47.25$ m at an azimuth angle of $\psi = 90°$, but with

different preview distances (D = 24, 58, and 130 m). The curves in Figure 11 and Figure 12 do not include the effects of *uv* or *uw* correlation in order to highlight the other sources of coherence loss. Although the exact measurement curves differ for the two wind field models, the following trends apply to both scenarios. When D = 24 m, the measurement angle is large, longitudinal coherence (dashed) is relatively high, and the effects of range weighting are insignificant due to the short focal distance. Here, directional bias dominates the overall coherence, with wind evolution causing some degradation at higher frequencies. When D = 130 m, the measurement angle is low, longitudinal coherence is low, due to wind evolution, and range weighting is significant due to the long focal distance. Wind evolution is the dominant component of measurement coherence, with range weighting adding a further loss of coherence. For the D = 58 m scenario, all three sources of coherence loss are significant. Directional bias and wind evolution both have very strong impacts, with range weighting causing an additional loss of coherence.

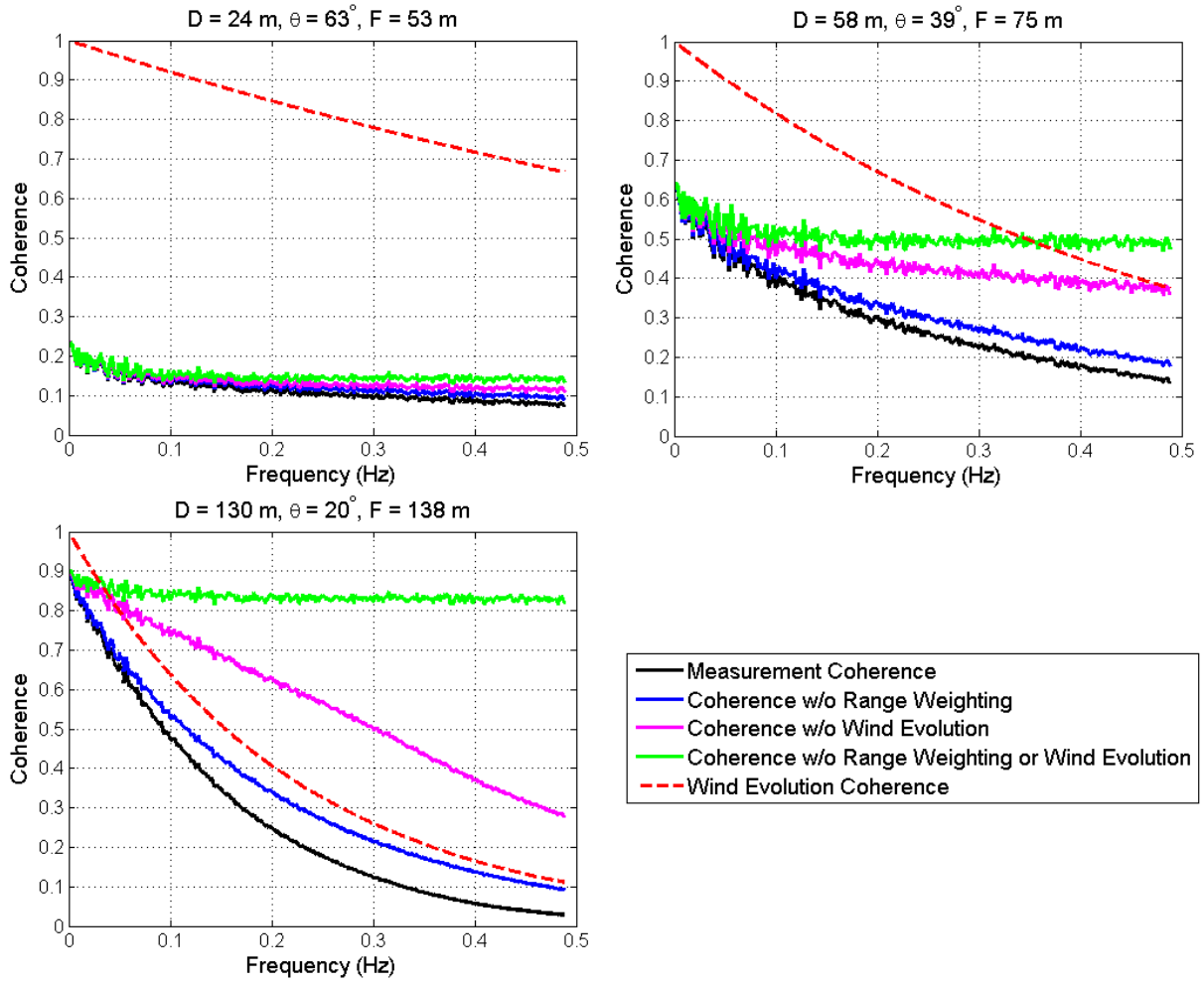

Figure 11. A comparison of the components of measurement coherence for a scanning LIDAR scenario, with r = 47.25 m using the Great Plains-Low Level Jet wind field and exponential coherence with a = 0.45

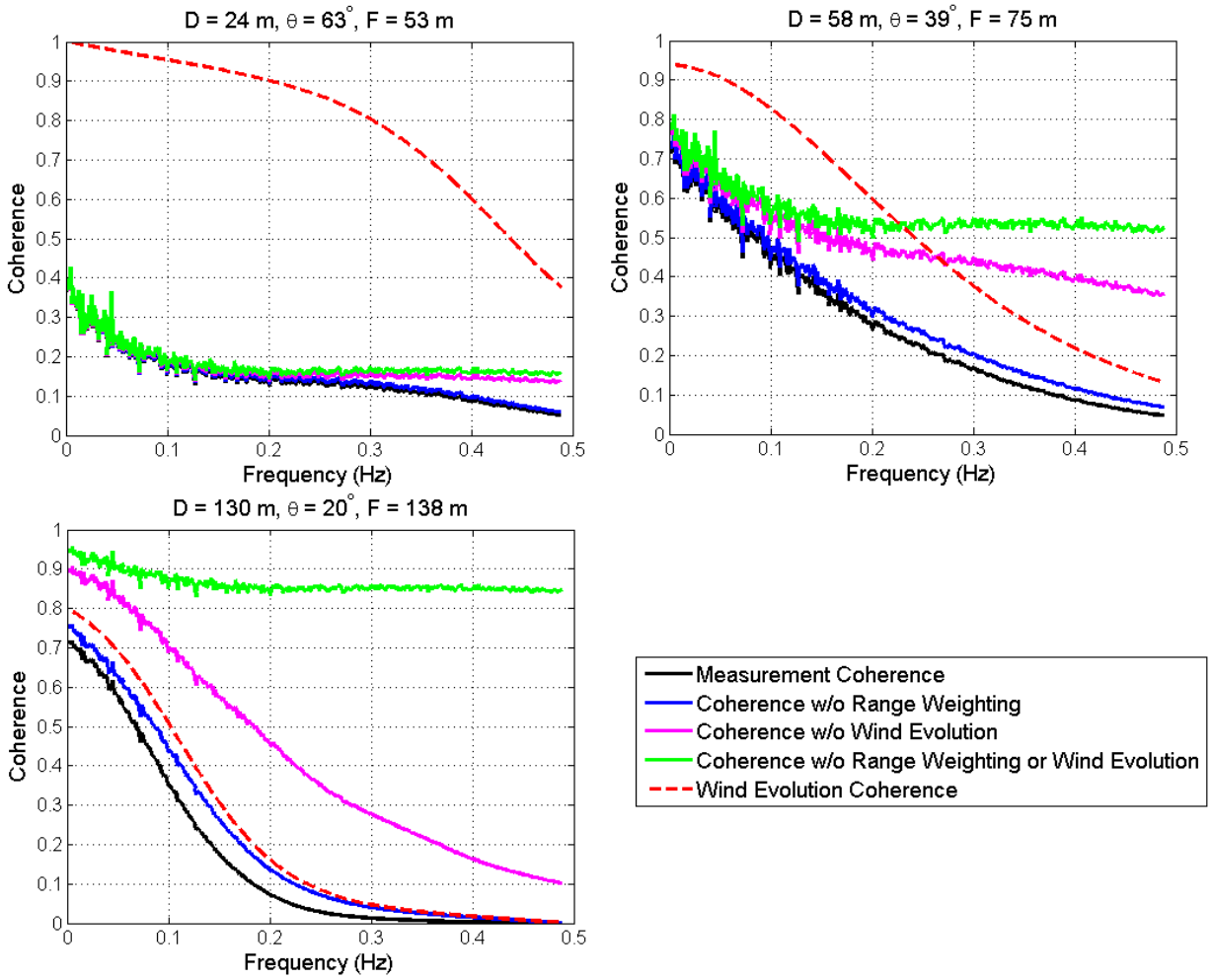

Figure 12. A comparison of the components of measurement coherence for a scanning LIDAR scenario with *r* = 47.25 m using the stable LES wind field and evolution model

Figure 11 and Figure 12 reveal that the (green) coherence curves from directional bias alone are relatively constant over all frequencies and increase as the measurement angle decreases. Although not shown in Figure 11 or Figure 12, when the effects of *uv* and *uw* coherence (present in the Great Plains-Low Level Jet wind field) are included, measurement coherence, due to directional bias, changes because of the non-zero correlation between the *u* and *v* as well as *u* and *w* components. This behavior can be explained through Eqs. 5.11 and 5.16. By comparing the green and magenta curves, it can be seen that range weighting adds a significant coherence loss when wind evolution is not included, especially for larger preview distances. However, by comparing the blue and black curves, it is clear that with wind evolution included, range weighting never dominates the overall coherence loss.

6 LIDAR Measurements of Evolving Wind Fields

In this study, researchers assessed the measurement quality of realistic scanning patterns using a Light Detection and Ranging (LIDAR) system. For this, the Great Plains-Low Level Jet wind field, along with the exponential coherence model, was used to represent an unstable boundary layer. The large eddy simulation (LES) was used to represent a model of a weakly stable boundary layer. Similar to the results for scanning LIDAR performance in frozen wind fields that are discussed in Section 2.3, measurement quality is examined for different scan radii as a function of preview distance. However, instead of using root mean square (RMS) error to judge measurement quality, here the metrics are based on the coherence between the measured wind and the wind that reaches the rotor, as described in equation (Eq.) 5.1. Measurement coherence is calculated directly, using the formulas outlined in Section 5, without performing computationally expensive and memory intensive time-domain simulations of LIDAR measurements in evolving wind fields.

Two metrics are used to reveal the measurement quality for different scan geometries. The first metric is the "coherence bandwidth," defined here as the bandwidth where the measurement coherence remains above 0.5. A higher coherence bandwidth yields a better measurement, because more of the measured turbulence spectrum can be used in a wind preview-based controller. The second metric is the integral of measurement coherence, or the area under the coherence curve. The integration is only performed for a bandwidth of about 0.5 hertz (Hz), based on the Nyquist frequency of the LES wind field. A larger area under the coherence curve will yield a better measurement. Results based on the two metrics are similar, but both are provided here for comparison.

The following results compare measurement quality for different scan geometries and reveal the optimal preview distances in terms of maximizing the coherence bandwidth or coherence integration. For the exponential wind evolution model, the decay parameter a is varied to show the impact that wind evolution intensity has on optimal preview distance. For the LES-based model, the results reveal what typical preview distances might be in a stable wind field with physics-based wind evolution, but a wind field that is less productive from a wind energy perspective. Separate results are provided for four different LIDAR azimuth angles (ψ = 0°, 90°, 180°, -90°) because the wind spectra and transverse coherences vary with height and direction. In addition, for the TurbSim generated wind field, the uv and uw correlations will have different impacts on measurement coherence (depending on azimuth angle).

The chosen scan geometries are based on the National Renewable Energy Laboratory (NREL) 5-megawatt (MW) turbine model. Scan radii of 15.75 meters (m), 31.5 m, 47.25 m, and 63 m are investigated, which correspond to 25%, 50%, 75%, and 100% blade span. For the Great Plains-Low Level Jet scenario, the LIDAR is located at a height of 90 m, but for the LES wind field, the LIDAR is located at a height of 100 m, which is the center of that wind field.

6.1 Measurements Using the Exponential Wind Evolution Model

For the TurbSim wind field with the exponential wind evolution model, results are provided for ψ = 90° and ψ = -90°, where the LIDAR is only measuring wind in the xy plane, ψ = 0°, where

the LIDAR is measuring wind in the *xz* plane above hub height, and $\psi = 180°$, where wind is measured in the *xz* plane below hub height. These four azimuth angles were chosen because the wind spectra and transverse coherences are different in the *y* and *z* directions. In addition, l_y will be positive for $\psi = 90°$ and negative for $\psi = -90°$. Similarly, l_z will be positive for $\psi = 0°$ and negative for $\psi = 180°$. This allows the researchers to investigate the impact of *uv* and *uw* cross-correlations in Eqs. 5.11 and 5.16, for both positive and negative l_y and l_z components. Furthermore, the spectra and transverse coherence curves vary with height, so measurements above and below hub height are analyzed.

Figure 13 compares the $\gamma^2 = 0.5$ coherence bandwidths of measurement coherence as a function of preview distance for a range of decay parameters. Note that the green curves represent a decay parameter $a = 0$, which is equivalent to no wind evolution (Taylor's frozen turbulence hypothesis). Coherence bandwidth curves are provided for the four different azimuth angles. For shorter scan radii, the preview distances that provide maximum coherence bandwidth are shorter, because the degradation caused by directional bias that enters the coherence calculations through Eq. 5.11 is lower than for larger scan radii. Therefore, with small scan radii, the dominant source of coherence loss transitions from directional bias to wind evolution or range weighting at shorter preview distances.

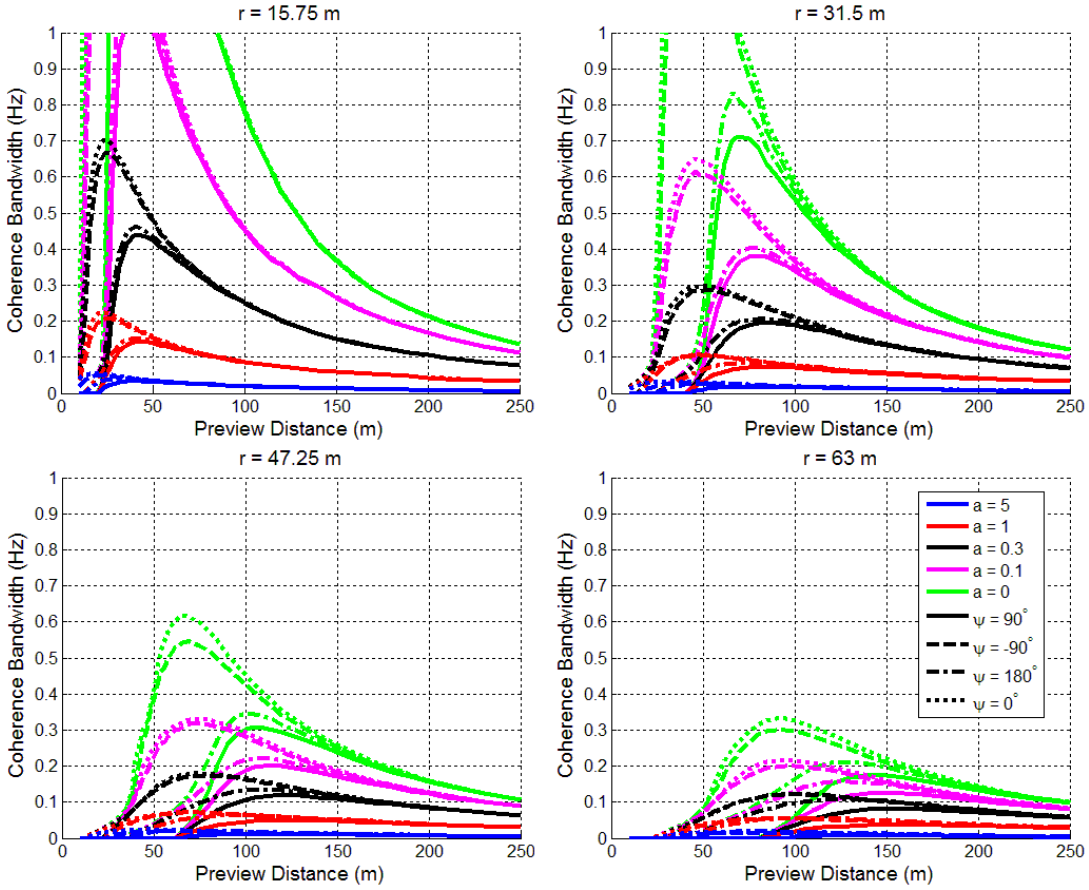

Figure 13. This figure shows the $\gamma^2 = 0.5$ coherence bandwidth versus preview distance for the Great Plains-Low Level Jet wind field for scan radii of $r = 15.75$ m, 31.5 m, 47.25 m, and 63 m. The wind evolution is based on an exponential coherence model with various decay parameters.

In Figure 13, the curves for azimuth angles $\psi = 90°$ and $\psi = 180°$ are very similar, as are the curves for azimuth angles $\psi = 0°$ and $\psi = -90°$. For $\psi = 90°$ and $\psi = 180°$, the cross-power spectral densities (CPSDs), between the *u* and *v* as well as the *u* and *w* components, introduce a negative contribution in Eqs. 5.11 and 5.16. This behavior is due to l_y and $S_{uv}(f)$ both having positive signs and l_z and $S_{uw}(f)$ both having negative signs. The negative contribution of the *v* and *w* components causes a reduction in both the magnitude of the measured LIDAR signal and the overall measurement coherence. In contrast, for $\psi = -90°$ and $\psi = 0°$, l_y is negative while the sign of $S_{uv}(f)$ is positive, and l_z is positive while the sign of $S_{uw}(f)$ is negative. Therefore, the CPSDs, between the *u* and *v* as well as the *u* and *w* components, introduce a positive contribution in Eqs. 5.11 and 5.16. The positive contribution of the *v* and *w* components causes an increase in both the magnitude of the measured LIDAR signal and the overall measurement coherence.

Although the influence of the *uv* and *uw* cross-correlations is the main factor contributing to the azimuthal dependence of measurement coherence, further variations between the curves for different azimuth angles in Figure 13 reveal how the relative magnitudes of the wind spectra components affect measurement coherence. Measurements at an azimuth angle of $\psi = 0°$ in the *xz* plane produce slightly higher coherence bandwidths than measurements at $\psi = -90°$ in the *xy* plane. Likewise, measurements at an azimuth angle of $\psi = 180°$ in the *xz* plane produce higher coherence bandwidths than measurements at $\psi = 90°$ in the *xy* plane. The improved results for the measurements in the *xz* plane can be explained by examining the wind spectra in Figure 6. The ratio between the *v* component of the wind spectrum and the *u* component is greater than the ratio between the *w* and *u* components at all heights, so the *v* component of the wind corrupts measurements more than the *w* component. Therefore, when measurements are confined to the *xy* plane, there is more coherence loss due to directional bias effects than when measurements are confined to the *xz* plane.

Figure 14 shows results for the same measurement scenarios as in Figure 13, but with the integral of the coherence curves as the measurement quality metric. Most of the trends are similar to those in Figure 13, but with slightly different optimal preview distances.

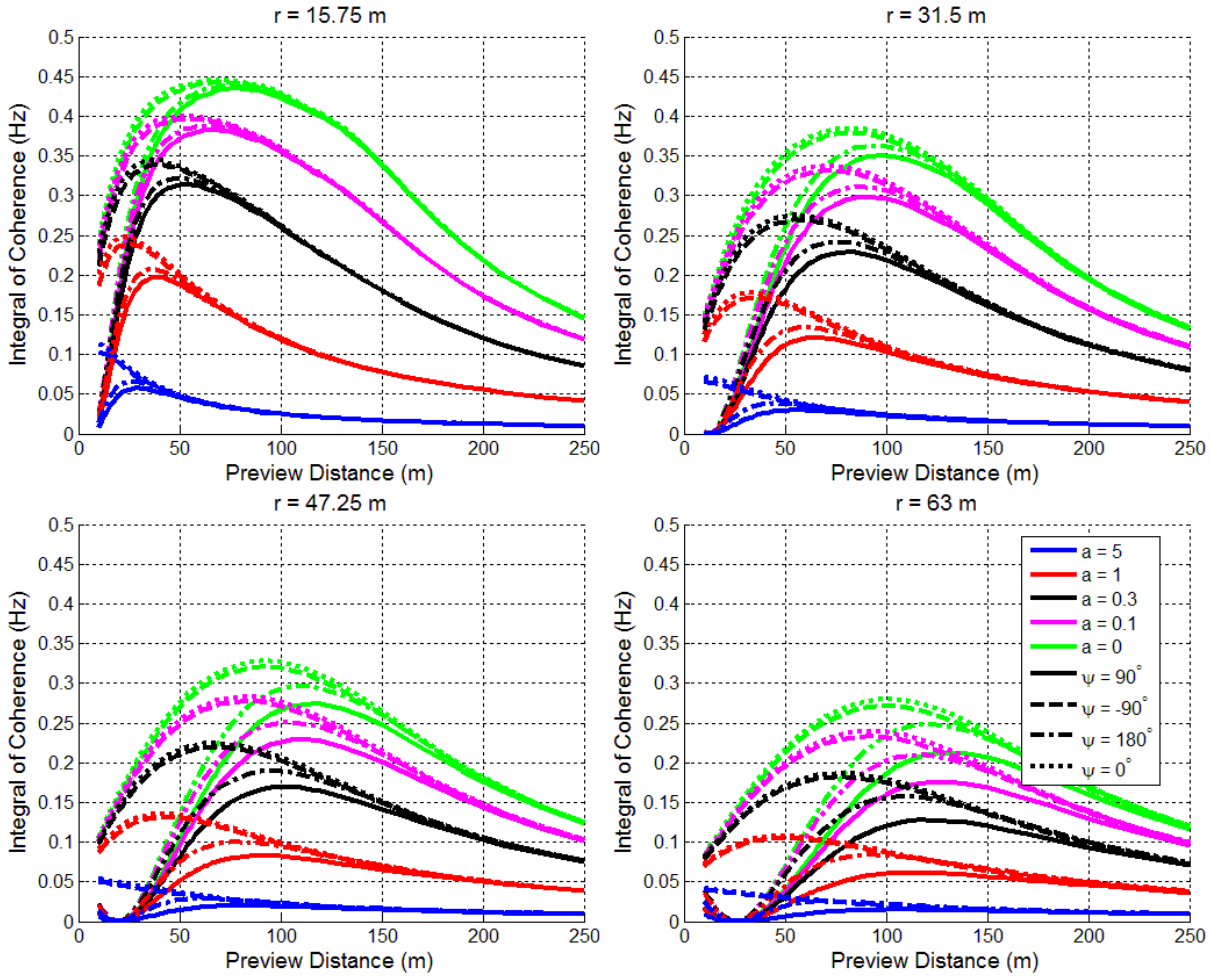

Figure 14. Integral of measurement coherence from 0 hertz (Hz) to 0.5 Hz versus preview distance for the Great Plains-Low Level Jet wind field for scan radii of *r* = 15.75 m, 31.5 m, 47.25 m, and 63 m. Wind evolution is based on an exponential coherence model with various decay parameters.

While the maximum coherence bandwidths are much lower for larger decay parameters, as can be expected, interestingly, the optimal measurement preview distances do not change very much as *a* is varied when using the coherence bandwidth metric. When using the integral of coherence as a metric, the optimal preview distance is much more sensitive to changes in the decay parameter. Figure 15 and Figure 16 show the optimal preview distance as a function of decay parameter for the four azimuth angles at the four scan radii, when the quality metrics are the coherence bandwidth and the integral of the coherence curve, respectively. Also shown in these plots are the maximum bandwidths and integrals achieved at the optimal preview distances. Instead of decreasing monotonically as the wind evolution intensity increases, as might be expected, the optimal preview distances that are based on coherence bandwidth become greater as the decay parameter is increased, up until a certain point where they begin to decrease. For both metrics, there is a considerable difference between the optimal preview distances for the different azimuth angles. This spread in optimal preview distance suggests that, for azimuth angles where directional bias effects are less severe due to positive cross-correlations or weaker transverse *v* and *w* wind components, the optimal preview distance is shorter.

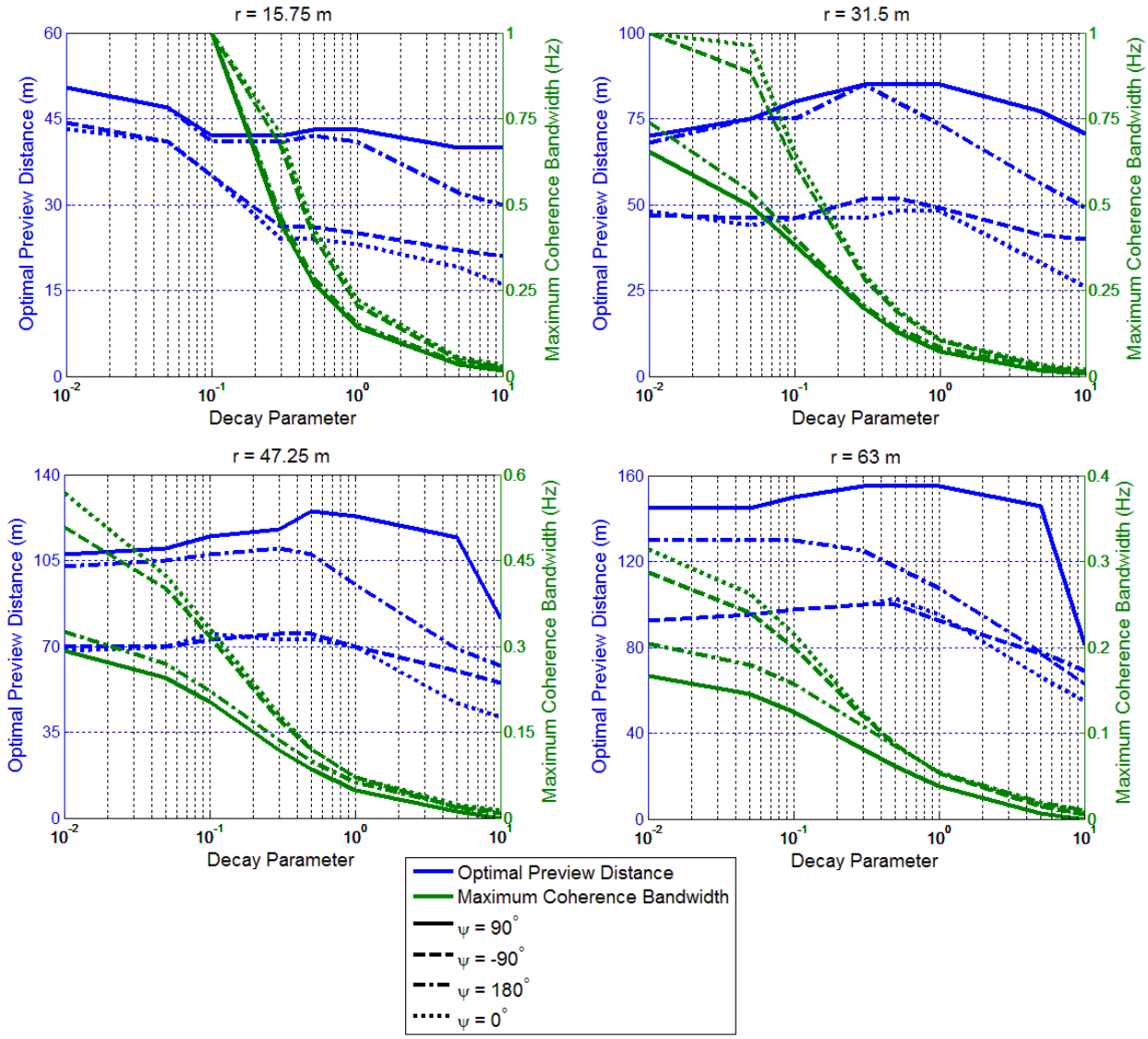

Figure 15. Maximum γ^2 = 0.5 coherence bandwidth preview distance versus decay parameter for the Great Plains-Low Level Jet wind field using the exponential wind evolution model for scan radii of *r* = 15.75 m, 31.5 m, 47.25 m, and 63 m. Corresponding maximum coherence bandwidths are shown using a secondary axis (right) in green.

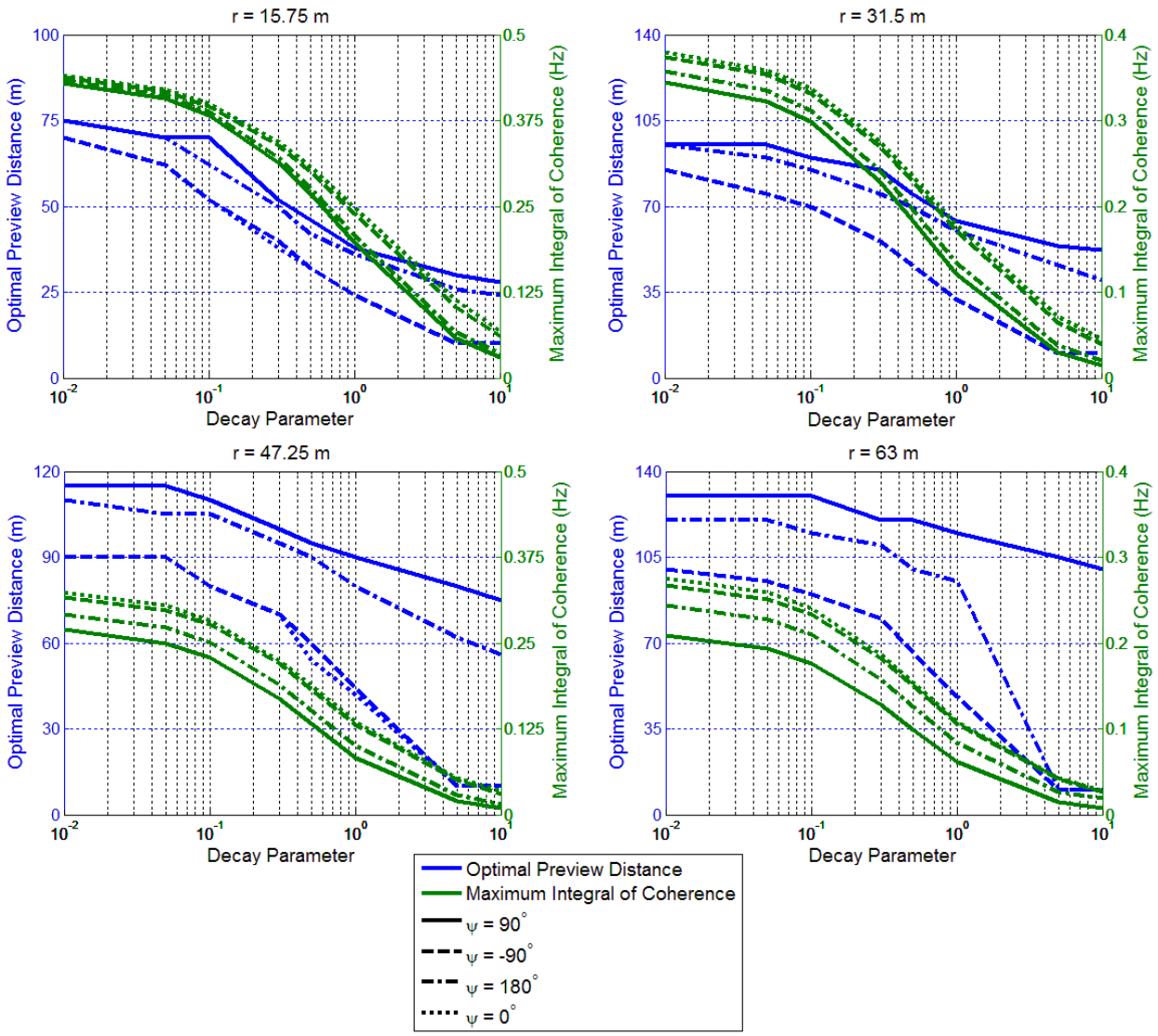

Figure 16. The optimal preview distance is shown here, based on integral of measurement coherence versus decay parameter for the Great Plains-Low Level Jet wind field using the exponential wind evolution model for scan radii of *r* = 15.75 m, 31.5 m, 47.25 m, and 63 m. Corresponding maximum integrals of measurement coherence from 0 Hz to 0.5 Hz are shown using a secondary axis (right) in green.

6.2 Measurements Using the LES Wind Evolution Model

For the LES wind field, results are provided for $\psi = 90°$, where the LIDAR is only measuring wind in the *xy* plane, $\psi = 0°$, where the LIDAR is measuring wind in the *xz* plane above hub height, and $\psi = 180°$, where wind is measured in the *xz* plane below hub height. These three azimuth angles were chosen because the wind spectra and transverse coherences are different in the *y* and *z* directions. The "cross-correlations" between the *u* and *v* and *u* and *w* components are not included in the LES spectral model used in this research. Therefore, an azimuth angle of $\psi = -90°$ would produce the same coherence as $\psi = 90°$, and only the $\psi = 90°$ scenario is included. An additional simplification used during the LES-based measurement coherence calculations is treating the coherence between arbitrary points in the wind field as the product between the coherence curves resulting from the measured transverse and longitudinal separations.

Using the spectral statistics determined from the stable LES wind field, coherence bandwidths and coherence integrals are examined in Figure 17 and Figure 18 for different measurement geometries. For the LES-based results, there is less of a difference between measurements at the three azimuth angles because the effects of *uv* and *uw* correlations are not included. The highest levels of coherence are achieved with $\psi = 0°$, and the lowest coherence results from measurements with $\psi = 90°$. The azimuth angle of $\psi = 180°$ produces coherence levels between the two extremes. These differences can be explained by the relative magnitudes of the *u*, *v*, and *w* components of the wind spectra at different heights, as shown in Figure 8.

When $\psi = 0°$ and $\psi = 180°$, the estimate of the *u* component, based on a line-of-sight measurement, is corrupted by the *w* component of wind. The ratio of the *w* component of the wind spectra to the *u* component is higher for lower heights, which explains why measurements at the azimuth angle of $\psi = 180°$ produce lower coherence levels than those at the azimuth angle of $\psi = 0°$. For the azimuth angle of $\psi = 90°$, the estimate of the *u* component is corrupted by the *v* component of the wind. At a height of $z = 100$ m, the ratio of the *v* component of the wind spectrum to the *u* component is higher than the *w* to *u* component ratio when $\psi = 0°$ and $\psi = 180°$. This explains why the $\psi = 90°$ produces the lowest measurement coherence of all three azimuth angles. Another factor that might impact the measurement coherence levels is the lower transverse coherence curve levels in the *z* direction than in the *y* direction, as shown in Figure 9.

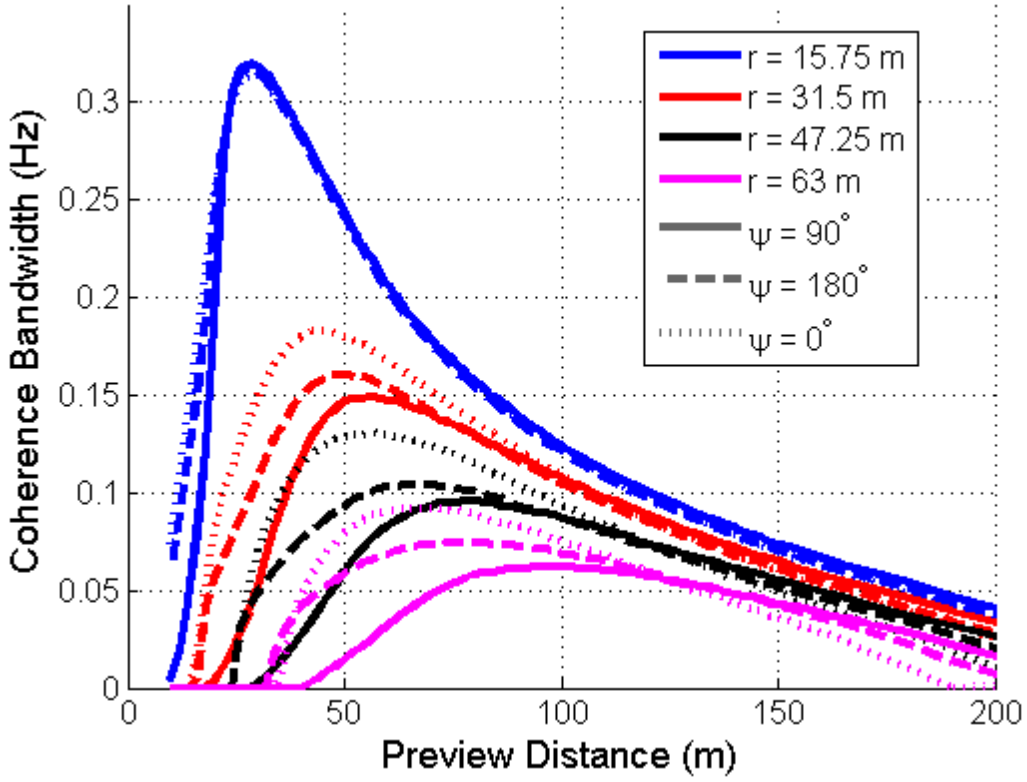

Figure 17. The $\gamma^2 = 0.5$ coherence bandwidth versus preview distance for the stable LES wind field is shown here, for scan radii of $r = 15.75$ m, 31.5 m, 47.25 m, and 63 m

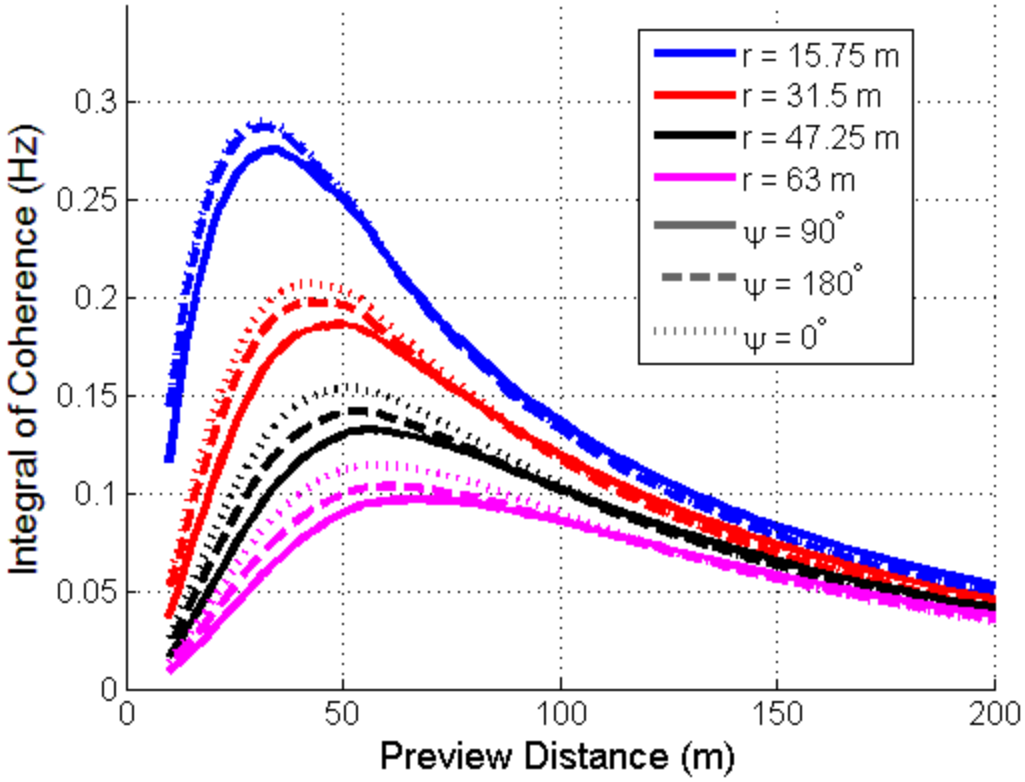

Figure 18. Integral of measurement coherence from 0 Hz to 0.5 Hz versus preview distance for the stable LES wind field for scan radii of *r* = 15.75 m, 31.5 m, 47.25 m, and 63 m

7 Conclusions and Future Work

In this report, we have explained how wind evolution can be described by longitudinal coherence functions in a wind field. Researchers examined the coherence between Light Detection and Ranging (LIDAR) system measurements and true wind speeds in evolving wind fields for realistic preview measurement scenarios. Wind evolution was introduced to a frozen wind field that is characteristic of the U.S. Great Plains, using a simple exponential model of longitudinal coherence that is a function of the non-dimensional value kD. A large eddy simulation (LES) of a stable boundary layer was used to derive both transverse and longitudinal coherence functions. Using wind spectra and coherence functions determined from the Great Plains-Low Level Jet wind field, researchers calculated measurement coherence directly, without having to perform computationally expensive and memory intensive simulations of LIDAR measurements in evolving wind fields.

Measurement coherence loss is dominated by the directional bias source of error for short preview distances as the result of high measurement angles. Further, the coherence is sensitive to both the cross-correlation of the wind components as well as the relative magnitudes of the transverse (v and w) and longitudinal (u) components of wind speed. As preview distance increases, the main source of coherence loss transitions to wind evolution. Figure 11 and Figure 12 show how LIDAR range weighting is not the dominant source of coherence loss when wind evolution is introduced, but it can have a significant impact when the intensity of wind evolution is low and the preview distance is large.

For the Great Plains wind field, with the exponential decay form of longitudinal coherence, it was found that varying the intensity of wind evolution by adjusting the decay parameter affects the measurement coherence considerably. However, using coherence bandwidth as a metric, it was revealed that, for a given scan radius, the optimal preview distance is not very sensitive to the amount of wind evolution. When using the area under the coherence curve as a metric, the optimal preview distance for a given scan radius is more sensitive to changes in the decay parameter.

Based on the results from Section 6, optimal preview distances, based on coherence bandwidth for LIDAR measurements in the unstable Great Plains wind field, are roughly 60 meters (m) for a scan radius of r = 31.5 m, 80 m for r = 47.25 m, and 120 m for r = 63 meters for decay parameters less than one. These approximate optimal preview distances are formed by averaging over all four azimuth angles. Using the integral of coherence as a metric, the optimal preview distances vary considerably as the decay parameter changes. Optimal preview distances, using root mean square (RMS) error as the metric in a frozen wind field with the same spectral characteristics (Figure 4), are around 115 m, 150 m, and 225 m, for scan radii of r = 31.5 m, r = 47.25 m, and r = 63 m, respectively. While the exact preview distances vary, depending on the metric used, and with wind evolution introduced, optimal preview distances that are based on coherence bandwidth are roughly half of those in frozen wind fields that are based on RMS error. However, when comparing results based on coherence bandwidth for different decay parameters, it can be seen that unless the intensity of evolution is very strong, the optimal preview distances are almost the same with wind evolution or without (when the decay parameter a = 0).

Results from Section 6 using the stable LES-based spectral model reveal that optimal preview distances based on coherence bandwidth, averaged over all three azimuth angles, are roughly 50 m for a scan radius of r = 31.5 m, 65 m for r = 47.25 m, and 80 m for r = 63 m. The optimal preview distances for the LES wind field are shorter than those for the TurbSim wind field, with exponential wind evolution at a given scan radius. A likely explanation for this trend is that the longitudinal coherence curves calculated from the LES wind field decrease in value much faster as a function of longitudinal separation than the coherence curves (based on the exponential function) do. As a result, wind evolution takes over as the dominant source of measurement coherence loss much faster as a function of preview distance using the LES-based wind evolution model than when using an exponential decay form of coherence. From a controls perspective, a preview measurement at 47.25 m, or 75% rotor radius for the 5-megawatt (MW) model, is the most useful due to maximum power capture near this blade span. The results in Figure 17 reveal that the bandwidth of coherent measurements at r = 47.25 m is roughly 0.11 hertz based on the $\gamma^2 = 0.5$ bandwidth definition.

Although not discussed in this report, an additional source of error in wind speed measurements is the effect of the induction zone upwind of the rotor. The induction zone, which extends roughly one rotor diameter in front of the turbine, has the effect of slowing down the advection velocity of the wind near the rotor, thereby deflecting the streamlines around the rotor disc by some amount and distorting the turbulence. The impact of the induction zone on wind speed measurements is an area of future study.

References

1. Laks, J.; Pao, L.; Wright, A.; Kelley, N.; Jonkman, B. "The Use of Preview Wind Measurements for Blade Pitch Control," *IFAC J. Mechatronics*, Vol. 21, No. 4, June 2011, pp. 668-681.

2. Dunne, F.; Pao, L.; Wright, A.; Jonkman, B.; Kelley, N. "Adding Feedforward Blade Pitch Control to Standard Feedback Controllers for Load Mitigation in Wind Turbines," *IFAC J. Mechatronics*, Vol. 21, No. 4, June 2011, pp. 682-690.

3. Schlipf, D.; Kühn, M. "Prospects of a Collective Pitch Control by Means of Predictive Disturbance Compensation Assisted by Wind Speed Measurements," in *Proc. German Wind Energy Conference (DEWEK)*, Bremen, Germany, November 2008.

4. Schlipf, D.; Trabucchi, D.; Bischoff, O.; Hofsäß, M.; Mann, J.; Mikkelsen, T.; Rettenmeier, A.; Trujillo, J.; Kühn, M. "Testing of Frozen Turbulence Hypothesis for Wind Turbine Applications with a Scanning LIDAR System," in *Proc. International Symposium for the Advancement of Boundary Layer Remote Sensing*, Paris, France, June 2010.

5. Laks, J.; Pao, L.; Simley, E.; Wright, A.; Kelley, N.; Jonkman, B. "Model Predictive Control Using Preview Measurements from LIDAR," in *Proc. 49th AIAA Aerospace Sciences Meeting*, Orlando, FL, January 2011.

6. Dunne, F.; Pao, L.-Y.; Wright, A.D.; Jonkman, B.; Kelley, N.; Simley, E. "Adding Feedforward Blade Pitch Control for Load Mitigation in Wind Turbines: Non-causal Series Expansion, Preview Control, and Optimized FIR Filter Methods," in *Proc. 49th AIAA Aerospace Sciences Meeting*, Orlando, FL, January 2011.

7. Taylor, G.I. "The Spectrum of Turbulence," *Proc. Roy. Soc. Lond. A,* Vol. 164, pp. 476-490, 1938.

8. Simley, E.; Pao, L.-Y.; Frehlich, R.; Jonkman, B.; Kelley, N. "Analysis of Wind Speed Measurements Using Coherent LIDAR for Wind Preview Control," in *Proc. AIAA Aerospace Sciences Meeting*, Orlando, FL, January 2011.

9. Medici, D.; Ivanell, S.; Dahlberg, J.-Å.; Alfredsson, P. "The Upstream Flow of a Wind Turbine: Blockage Effect," *Wind Energy*, Vol. 14, 2011, pp. 691-697.

10. Jonkman, B. "TurbSim User's Guide: Version 1.50," NREL/TP-500-46198, Golden, CO: National Renewable Energy Laboratory, 2009.

11. Beare, B.; MacVean, M.; Holtslag, A.; Cuxart, J.; Esau, I.; Golaz, J.; Jimenez, M.; Khairoutdinov, M.; Kosovic, B.; Lewellen, D.; Lund, T.; Lundquist, J.; McCabe, A.; Moene, A.; Noh, Y.; Raasch, S.; Sullivan, P. "An Intercomparison of Large-Eddy Simulations of the Stable Boundary Layer," *Boundary Layer Meteorology*, Vol. 118, No. 2, Dec. 2006, pp. 247-272.

12. Jonkman, J.; Butterfield, S.; Musial, W.; Scott, G. “Definition of a 5-MW Reference Wind Turbine for Offshore System Development,” NREL/TP-500-38060, Golden, CO: National Renewable Energy Laboratory, 2009.

13. Frehlich, R.; Kavaya, M. “Coherent Laser Performance for General Atmospheric Refractive Turbulence,” *Applied Optics*, Vol. 30, No. 36, December 1991, pp. 5325–5352.

14. Courtney, M.; Wagner, R.; Lindelöw, P. “Commercial Lidar Profilers for Wind Energy. A Comparative Guide,” in *Proc. European Wind Energy Conference*, Brussels, Belgium, April 2008.

15. Mikkelsen, T.; Hansen, K.; Angelou, N.; Sjöholm, M.; Harris, M.; Hadley, P.; Scullion, R.; Ellis, G.; Vives, G. “LIDAR Wind Speed Measurements from a Rotating Spinner,” in *Proc. European Wind Energy Conference*, Warsaw, Poland, April 2010.

16. Dunne, F.; Pao, L.; Wright, A.; Jonkman, B.; Kelley, N. “Combining Standard Feedback Controllers with Feedforward Blade Pitch Control for Load Mitigation in Wind Turbines,” in *Proc. 48th AIAA Aerospace Sciences Meeting*, Orlando, FL, January 2010.

17. Pielke, R.A.; Panofsky, H.A. “Turbulence Characteristics along Several Towers,” *Boundary Layer Meteorology*, Vol. 1, No. 2, 1970, pp. 115-130.

18. Schlipf, D. “Wind Turbine Control Using Lidar: Notes to Presentation,” in *PhD Summer School: Remote Sensing for Wind Energy*, Roskilde, Denmark, June 2011.